RSC Advances

PAPER

View Article Online
View Journal | View Issue

Cite this: *RSC Adv.*, 2025, **15**, 31176

Photoresponsive Cu-covalent organic polymer as multifunctional artificial enzyme for synergistic infected wound therapy

Chunzhen Zhao, †[ad] Changxiao Du,†[cd] Jie Xu,†[a] Yuqing Zhao,†[d] Xiaoming Shi,[e] Dong Zhang,[e] Xinmiao Zhang,[d] Yi Zhang,[d] Han Sun,[d] Xixin Jiang,[d] Zhen Du,[d] Mengjin Wang,[d] Meimei Xiao*[c] and Mingwen Zang*[bc]

The escalating challenges associated with antibiotic resistance have posed formidable obstacles in the fight against microbial infections and the prevention of biofilm formation. To address this challenge, we developed PEB-COP-Cu, a low-cost, readily available copper-integrated covalent organic polymer (COP) with dual enzyme-like activities and intrinsic photoresponsiveness, to accelerate infected wound healing. This material was synthesized through the post-metallization process of a COF xerogel (PEB-COP), obtained *via* a Michael addition elimination reaction, utilizing photoactive tetra-(4-aminophenyl) porphyrin (TAPP) and β-ketoenamine, specifically 1,3,5-tris(3-dimethylamino-1-oxoprop-2-en-yl) benzene (abbreviated as TDOEB), as the fundamental building blocks. PEB-COP-Cu enables multimodal antimicrobial action through integrated photothermal therapy (PTT) and type I/II photodynamic therapy (PDT), generating reactive oxygen species (ROS) in both oxygenated and hypoxic environments. This material demonstrates dual mimicking enzymatic activities (oxidase and peroxidase) to achieve ROS-mediated bacterial inactivation with or without H_2O_2. Specifically, under H_2O_2-deficient conditions, it catalyzes oxygen conversion to produce superoxide anions ($O_2^{\bullet-}$), while in H_2O_2-excess scenarios, it also depletes excessive H_2O_2 to enhance $^{\bullet}OH$ generation. The synergistic integration of these enzymatic cascades with PTT/PDT establishes a comprehensive antimicrobial system that operates through coordinated molecular mechanisms. This combined therapeutic strategy demonstrates threefold therapeutic advantages, which could effectively eradicate bacteria, inhibit biofilm formation, and promote wound healing *via* harnessing and modulating the infectious microenvironment (IME). Our findings establish PEB-COP-Cu as a pioneering therapeutic platform that simultaneously addresses the key challenges of conventional enzymatic therapy, achieving significantly improved biocidal efficacy while minimizing off-target cytotoxicity.

Received 28th June 2025
Accepted 12th August 2025

DOI: 10.1039/d5ra04493f

rsc.li/rsc-advances

Introduction

Skin, being the largest organ of the human body, holds a pivotal role in safeguarding internal tissues from external environmental harm.[1] Nevertheless, skin injuries, encompassing wounds, burns, and ulcers, not only inflict pain but also pave the way for infections, thereby prolonging or complicating the healing trajectory.[2] Hence, antibacterial treatment emerges as indispensable in the repair of infected skin injuries, as it efficiently thwarts the ingress of pathogens and expedites wound recovery.[3] However, traditional pharmacological treatment approaches confront formidable hurdles.[4] For example, the escalating resistance of infectious pathogens to existing medications has not only diminished treatment effectiveness, but also rendered certain common infections increasingly intractable.[5] Meanwhile, the protection of biofilm empowers the capacity with bacteria to withstand host immune, drastically aggregating the treatment difficulty. The pursuit of innovative therapeutic strategies, avoiding the evolution of bacteria to drug-resistance and the formation of biofilm, has become absolutely imperative to tackle this pressing global public health dilemma.

Photothermal therapy (PTT) and photodynamic therapy (PDT) are two primary noninvasive techniques harnessing the synergy of photosensitizers (PSs) and light sources to combat antimicrobial resistance.[6] PTT leverages the local hyperthermia

[a]*Affiliated Hospital of Shandong Second Medical University, Shandong Second Medical University, 261053 Shandong, PR China*
[b]*Weifang Brain Hospital, Weifang, Shandong, PR China*
[c]*Weifang People's Hospital, Shandong Second Medical University, Weifang, Shandong, PR China. E-mail: 511017186@qq.com; 806002570@qq.com*
[d]*School of Pharmacy, Shandong Second Medical University, Weifang, 261053 Shandong, PR China*
[e]*Shandong Neptunus Galaxy Pharmaceutical Co., Ltd, Weifang, Shandong, PR China*
† These authors contribute equal to this work.

to eliminate bacteria *via* the photothermal conversion realized by PSs upon absorbing specific light wavelengths.[7] To effectively eliminate bacteria, high temperatures are frequently necessary, along with substantial doses of medication.[8] However, this approach not only causes irreparable harm to normal cells, but also presents a significant challenge in achieving a balance between bacterial eradication and the preservation of healthy tissue.[9] PDT disrupts the cellular structure of pathogens by generating reactive oxygen species (ROS) catalyzed by the PSs under laser illumination.[10] However, the efficacy of PDT is significantly hampered by the concentration of oxygen, particularly in skin lesions where blood vessels are severely compromised, resulting in a treatment outcome falling short of expectations.[11]

Enzyme therapies are flourishing catalytic based antimicrobial model, which features the characteristics of high efficiency, specificity and low resistance.[12] However, the traditional enzyme therapy is concurrently challenged by the high preparation cost, as well as the intrinsic instability in both the structure and activity of natural enzymes under different media.[13] Artificial enzymes with the mimicking activity to the natural enzyme have emerged as alternatives for the enzyme therapy, which greatly boosting the development of enzyme therapy.[14] Peroxidase-like (POD-like) enzymes generally catalyze the decomposition of peroxides hydrogen (H_2O_2) to generate the toxic hydroxyl radicals ($^{\bullet}OH$) to kill bacteria.[15,16] Whereas, the real application of POD-like enzyme in the antimicrobial field is severely blocked by the limited activity in the IME, such as the low concentration of H_2O_2.[17]

Combination therapy realized by integrating different technologies, have stand out from the crowd to strength the efficacy of enzyme therapy at a low dose, but yield superior outcomes in antimicrobial therapy. For example, the combination of PTT with enzyme therapy.[18] Specifically, as a catalysis-based therapy, the reaction rate is significantly influenced by the reaction temperature. And the selective increase of the temperature at the lesion location has emerged as a focal point of current research to increase the enzyme activity.[19] However, the functional integration requires the design of appropriate materials *via* reasonable structure design. Therefore, it remains the difficulty of current research to seamlessly integrate diverse therapies into a platform maximizing the therapeutic effect.[20]

Covalent organic polymers (COPs), especially these with fully conjugated skeleton structure, exhibit distinctive features, such as exceptional chemical stability, and favorable biocompatibility, rendering them exceptionally suitable as PSs.[21] Meanwhile, the customizable structures and functions empower multiple functionality with COPs as ideal platform for the multimodal synergy therapy, optimizing therapeutic efficacy, while minimizing collateral damage to surrounding healthy tissues.[22] Nonetheless, the synthesis of COPs typically involves stringent conditions, necessitating meticulous control over reaction temperature and pressure, as well as the use of environmentally harmful corrosive solvents.[23] Currently, the targeted crafting of COPs with desirable functions under environmentally friendly and gentle conditions poses a significant challenge in contemporary research, especially those with customized multiple enzyme activities.

This study employs a green and low cost Michael addition–elimination reaction to synthesize the photoactive COP hydrogel using tetra-(4-aminophenyl)porphyrin (TAPP) and β-ketoenamine (1,3,5-tris(3-dimethylamino-1-oxoprop-2-en-yl) benzene, TDOEB) as building blocks. The reaction proceeds under ambient conditions in aqueous medium.[24] Lyophilization of the hydrogel yields PEB-COP with a fully conjugated skeleton, exhibiting superior photoactivity compared to TAPP. The coexistence of porphyrin chromophores and alkenylamine linkages in PEB-COP endows it with dual Cu^{2+} coordination sites, enabling POD-like and OXD-like functionalities upon Cu^{2+} chelation. This integration not only activates ROS generation for enhanced enzymatic therapy but also extends the conjugated system through Cu^{2+}-induced skeleton extension. Such structural modification broadens the light absorption spectrum, strengthens photothermal conversion efficiency, and consequently amplifies both PDT and PTT outputs. The synergistic effect of these photo-activated therapies establishes Por-EB-COP-Cu as a four-in-one antimicrobial platform. This work presents a green, facile synthetic strategy for developing multifunctional sterilizing agents, offering innovative solutions to improve infected wound management through IME modulation.

Results and discussion

Scheme 1 depicted the synthesis of Cu^{2+}-chelated antimicrobial agents (PEB-COP-Cu) through coordination with PEB-COP xerogel, obtained by lyophilizing the corresponding hydrogel. The PEB-COP hydrogel was efficiently prepared *via* a one-step Michael addition–elimination reaction using tetra-(4-aminophenyl)porphyrin (TAPP) and the C_3-symmetric β-ketoamine monomer 1,3,5-tris(3-dimethylamino-1-oxoprop-2-enyl) benzene (TDOEB) in aqueous solution under ambient conditions with acetic acid catalysis.[25] This method ensures maximal atom economy by utilizing hydrogel formation, thereby significantly reducing synthetic costs. Full experimental details including monomer characterization, hydrogel preparation protocols, and PEB-COP-Cu characterization are available in the SI.

The backbone structure of the PEB-COP and PEB-COP-Cu was concurrently characterized using Fourier Transform Infrared Spectroscopy (FT-IR) and solid-state ^{13}C Cross-Polarized Magic Angle Rotational Nuclear Magnetic Resonance (Solid-State ^{13}C NMR). The FT-IR spectrum (Fig. 1a) exhibited the disappearance of the stretching vibration of primary amine (3371 cm^{-1}) and N–CH_3 (1438 cm^{-1}) indexed to TAPP TDOEB, respectively, confirming the occurrence of the Michael addition–elimination reaction.[26,27] The emergence of the characteristic signal of secondary amine (Ar–NH) at approximately 1120 cm^{-1} verified the formation of alkenylamine linkages over the porous skeleton.[28] Meanwhile, the signals near 715 and 955 cm^{-1} corresponding to the Cu–O and Cu–N bonds confirmed the successful incorporation of Cu into the COP skeleton.[29,30] As shown in Fig. 1b, the solid-state ^{13}C

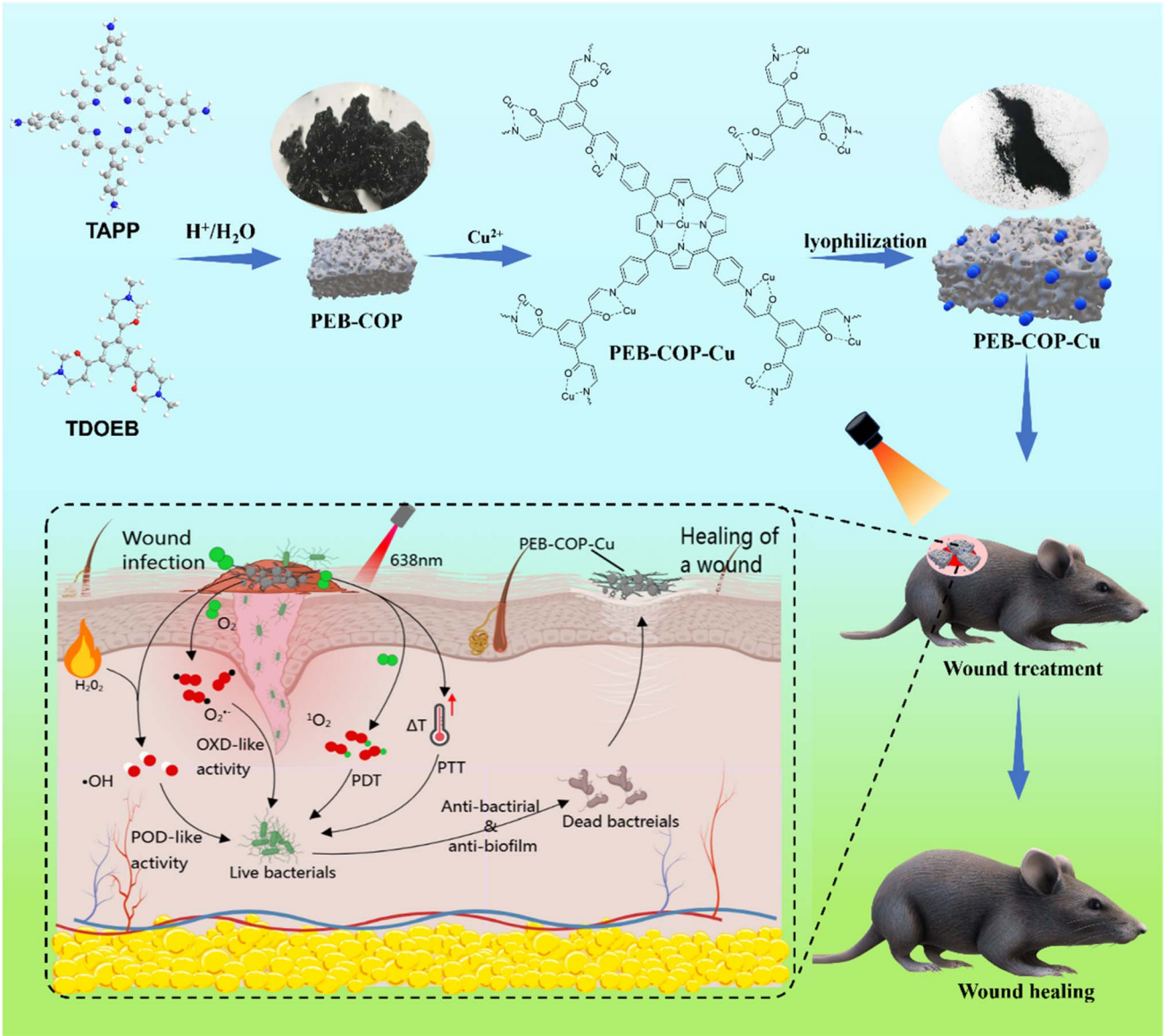

Scheme 1 Schematic route for the synthesis of PEB-COP-Cu and corresponding mechanism of wound healing promotion.

NMR spectrum of PEB-COP-Cu exhibited five distinct characteristic signals at 189, 138, 131, and 120 ppm, respectively. The characteristic peak observed at 138 ppm corresponded to the porphyrin-bridged carbon (c) (C–NH) and the α-carbon (a) of the carbonyl group in TDOEB.[31] The signals at 131 ppm and 120 ppm were identified as conjugated olefins in the porphyrin structure, whereas the residual resonance at 188 ppm was ascribed to the carbonyl carbon in the vinyl ketone portion of the (C=O).[32]

The X-ray photoelectron spectroscopy (XPS) was collected to explore the surface elemental composition of PEB-COP-Cu. The survey spectrum revealed the co-existence of characteristic peaks of C (53.73 at%), N (5.63 at%), O (30.44 at%) and Cu (10.21 at%) located at 284.8, 397.9, 531.6 and 934.7 eV, respectively (Fig. 1c). The high-resolution C 1s spectra was separated into 4 peaks with binding energy (BE) of 284.8, 286.2, 287.7 and 289.8 eV (Fig. 1d), They are attributed to C=C,C=N,C=O and πhe* bonds, respectively.[33] The N 1s spectrum was were fitted into 3 peaks with binding emerging of 397.9, 398.6 and 399.6 eV, belonging to the C–NH, C=N and N–Cu (Fig. 1e), respectively.[34] The O 1s spectrum of PEB-COP-Cu in Fig. 1f shows two peaks, one centred at 531.6 eV representing the C–O–Cu bond and the other centered at 532.9 eV representing the C=O bond.[35] Furthermore, the high resolution spectra of Cu 2p from PEB-COP-Cu indicate the coexistence of Cu(I) and Cu(II) substances on the sample surface. The Cu $2p_{3/2}$ XPS spectra were fitted and merged into two peaks at 935.1 and 933.7 eV, associated with Cu(II) and Cu(I), respectively. Similarly, the fitting of the Cu $2p_{1/2}$ XPS spectrum resulted in two peaks at 952.2 and 954.6 eV, associated with Cu(I) and Cu(II) substances, respectively (Fig. 1g).[33,36] These results unequivocally validated the successful preparation of PEB-COP-Cu. The

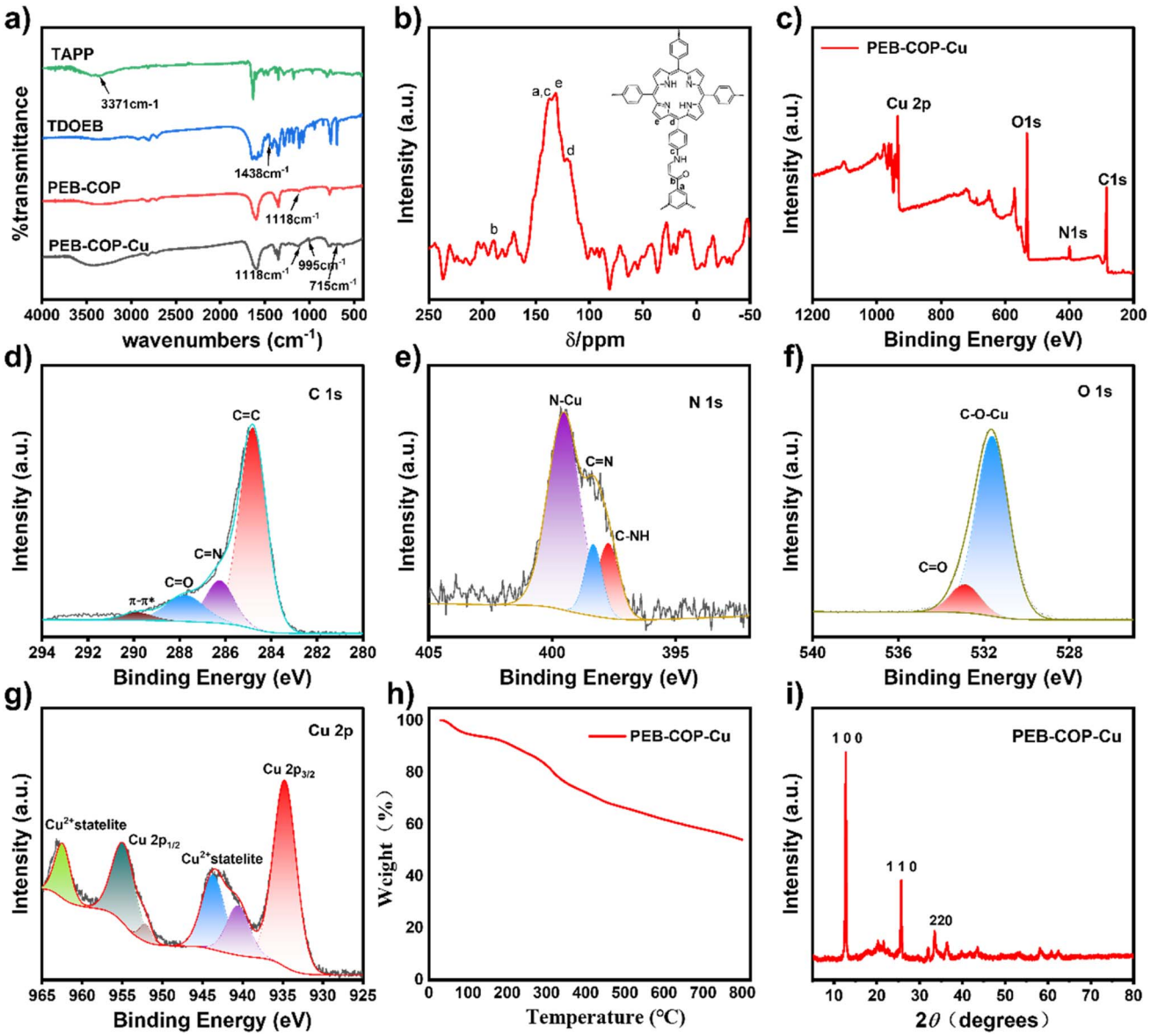

Fig. 1 (a) FT-IR patterns of TAPP, TDOEB, PEB-COP and PEB-COP-Cu; (b) ^{13}C CP/MAS NMR spectrum of PEB-COP-Cu; (c) XPS of PEB-COP-Cu; (d–g) XPS energy spectra of C 1s, N 1s, O 1s and Cu 2p, respectively; (h) weight loss of PEB-COP-Cu as a function of temperature; (i) X-ray diffractogram of PEB-COP-Cu.

thermogravimetric analysis (TGA) of PEB-COP-Cu (Fig. 1h) revealed PEB-COP-Cu were stable up to 200 °C with a tiny weight loss less than 5.0% below 100 °C attributed to the evaporation of water strongly absorbed in the heteroatom-rich porous skeleton. And a gradual mass loss was detected with the continuous increase of temperature. Remarkably, the material demonstrated exceptional thermal stability, retaining more than 58% of its initial mass even at elevated temperatures up to 800 °C.

The powder X-ray diffraction (XRD) patterns of the PEB-COP-Cu displayed obvious diffraction peaks at 12.5°, 25.7°, and 33.4°, corresponding to the (100), (110), and (220) crystal planes of the layer stacked skeleton (Fig. 1i).[37,38] Low temperature N_2 adsorption–desorption measurement was performed to investigate the inherent porosity of PEB-COP-Cu sample at 77 K. As shown in Fig. S1, PEB–COF–Cu exhibited a hierarchical pore structure dominated by both micropores and mesopores, as evidenced by its type II isotherm. The nearly vertical uptake observed at low pressure range ($P/P_0 < 0.0155$) clearly indicated the presence of micropores. Furthermore, the pronounced hysteresis loop appearing in the adsorption–desorption curves within the relative pressure range of $0.19 < P/P_0 < 0.96$ confirms the existence of mesopores.[39] The specific surface area (S_{BET}) of PEB-COP-Cu utilizing the Brunauer–Emmett–Teller (BET) method was determined to be 28.1 $m^2\ g^{-1}$ with a cumulative pore volume of 0.048 $cm^3\ g^{-1}$. Meanwhile, the pore size distribution (PSD) curve (Fig. S2) provided further evidence on the hierarchical pore structure with a main peak centered at 1.2 nm

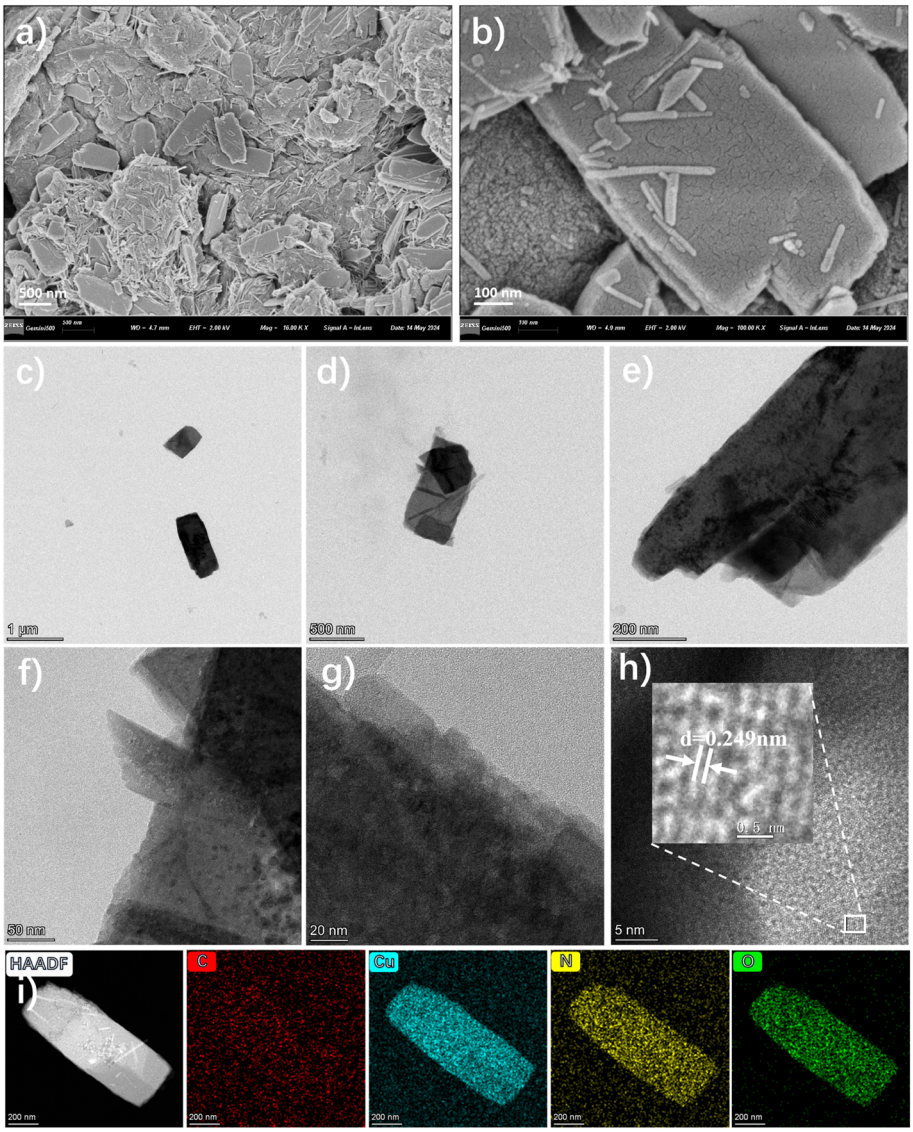

Fig. 2 The surface morphology and microstructure of PEB-COP-Cu. (a and b) SEM of PEB-COP-Cu at the scale bar of 500 and 100 nm, respectively; (c–g) TEM of PEB-COP-Cu at the scale bar of 1 μm, 500 nm, 200 nm, 50 nm and 20 nm, respectively; (h) high-resolution TEM of PEB-COP-Cu at scale bar of 5 nm; (i) EDS layered elemental mapping image of PEB-COP-Cu.

accompanying two secondary peaks located at 2.5 and 5.8 nm, respectively.

The hierarchical structure of PEB–COF–Cu was systematically characterized using scanning electron microscopy (SEM, Fig. 2a and b) and transmission electron microscopy (TEM, Fig. 2c–f). SEM images revealed a blocky aggregation morphology with a distinct layered lamellar assembly (Fig. 2a), while TEM observations demonstrated an interconnected porous network within the polymer skeleton (Fig. 2c). High-resolution TEM (HR-TEM, Fig. 2g and h) further revealed abundant micropores distributed throughout the framework, distinguishable by light/dark contrast (Fig. 2g). Notably, the inset HR-TEM image (Fig. 2h) showed ordered lattice stripes with a clear spacing of 0.249 nm, corresponding to the (100) plane of the layered structure.[40] Elemental mapping (Fig. 2i) and energy-dispersive X-ray spectroscopy (EDS, Fig. S3) confirmed homogeneous elemental distribution across the C-based matrix. Quantitative analysis yielded C (7.8%), N (0.25%), O (24.3%), and Cu (67.5%) contents, with Cu atoms preferentially localized in the porous regions.[41]

The fully conjugated structure and the specific compositions inspired us to investigate the optical physical performance of PEB-COP-Cu. Initially, the UV-Vis spectroscopic measurements were conducted to explore the optical absorption properties of PEB-COP-Cu (Fig. S4).[42] As seen, PEB-COP-Cu exhibited a broad-spectrum light absorption capability spanning from 200 to 800 nm with an extinction coefficient at 638 nm of 1.95×10^{-3} mL μg^{-1} cm^{-1}. Subsequently, the photothermal conversion capacity of PEB-COP-Cu was comprehensively evaluated by systematically monitoring the temporal temperature variations of the media *via* controlled altering either the material concentration or laser power density.[43] As illustrated in Fig. 3a,

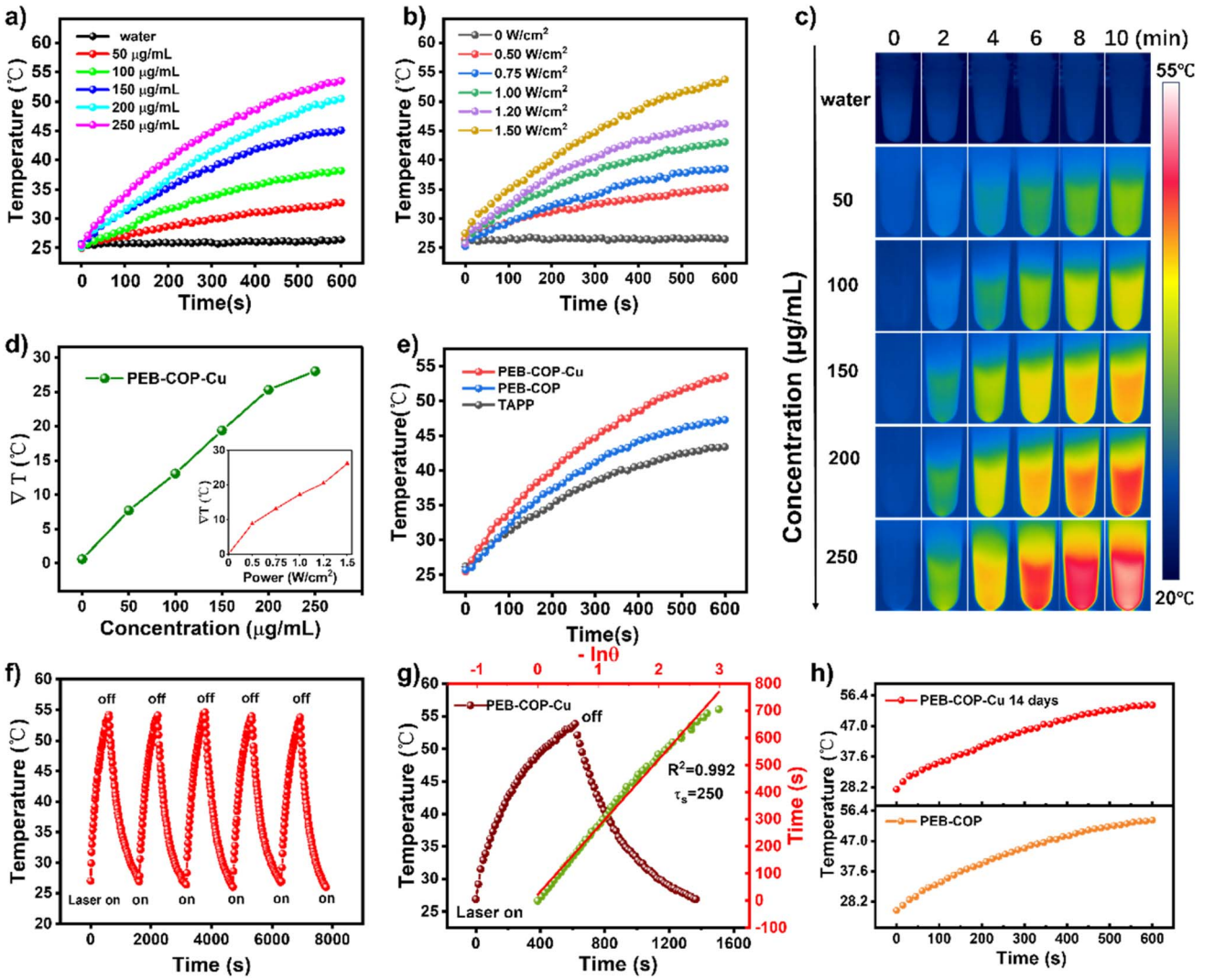

Fig. 3 Photothermal properties of PEB-COP-Cu under 638 nm laser irradiation: (a) Concentration-dependent photothermal effect; (b) photothermal response with laser power (250 μg mL^{-1}); (c) infrared thermal imaging of PEB-COP-Cu at different concentrations; (d) plots of maximum temperature change *vs.* concentration and laser powers (0.5–1.5 W cm^{-2}); (e) comparative photothermal curves of PEB-COP-Cu, PEB-COP and TAPP (250 μg mL^{-1}, 1.5 W cm^{-2}); (f) photothermal profiles of PEB-COP-Cu (250 μg mL^{-1}) in five cycles; (g) temperature profiles of PEB-COP-Cu (250 μg mL^{-1}) under laser irradiation (1.5 W cm^{-2}) and negative natural logarithms of the cooling cycles and temperatures; (h) temperature increase profiles of PEB-COP-Cu aqueous suspensions before/after 14 days of incubation in water.

PEB-COP-Cu exhibited concentration-dependent photothermal heating performance under 638 nm laser irradiation (1.5 W cm^{-2}). The temperature elevation (ΔT) of aqueous dispersions increased progressively from 7.7 to 28.0 °C with concentration escalation from 50 to 250 μg mL^{-1} during 10 min irradiation, while the control aqueous solution maintained negligible temperature fluctuations. Fig. 3b demonstrated a positive correlated relationship between laser power density (0.5–1.5 W cm^{-2}) and temperature rise. For a PEB-COP-Cu suspension (250 μg mL^{-1}), the temperature increased from 26.5 °C to 35.3, 38.5, 43.1, 46.2, and 53.7 °C, as the laser power increase from 0.5 to 0.75, 1.0, 1.25 and 1.5 W cm^{-2}, respectively. The dose-dependent photothermal behavior of PEB-COP-Cu was investigated using infrared thermography (Fig. 3c). As expected, higher concentrations of PEB-COP-Cu exhibited proportional temperature elevation, with maximal heating observed at 250 μg mL^{-1}.

The dose- and laser power-dependent photothermal response of the PEB-COP-Cu could also be intuitively observed from the plots of peak temperature rise with the variation of concentrations and laser powers, from which nearly linear relationship were evident (Fig. 3d). To elucidate the role of Cu^{2+} coordination, we compared the photothermal performance of PEB-COP-Cu with PEB-COP and TAPP under identical conditions (250 μg mL^{-1}, 638 nm, 1.5 W cm^{-2}, 10 min). As shown in Fig. 3e, a notable disparity was observed in the photothermal performance of the PEB-COP-Cu compared with the pristine COP and pure TAPP, where the PEB-COP-Cu demonstrated a much superior warming capability (53.7 °C *vs.* 47.3 °C for PEB-COP and 43.4 °C for TAPP). This superior performance

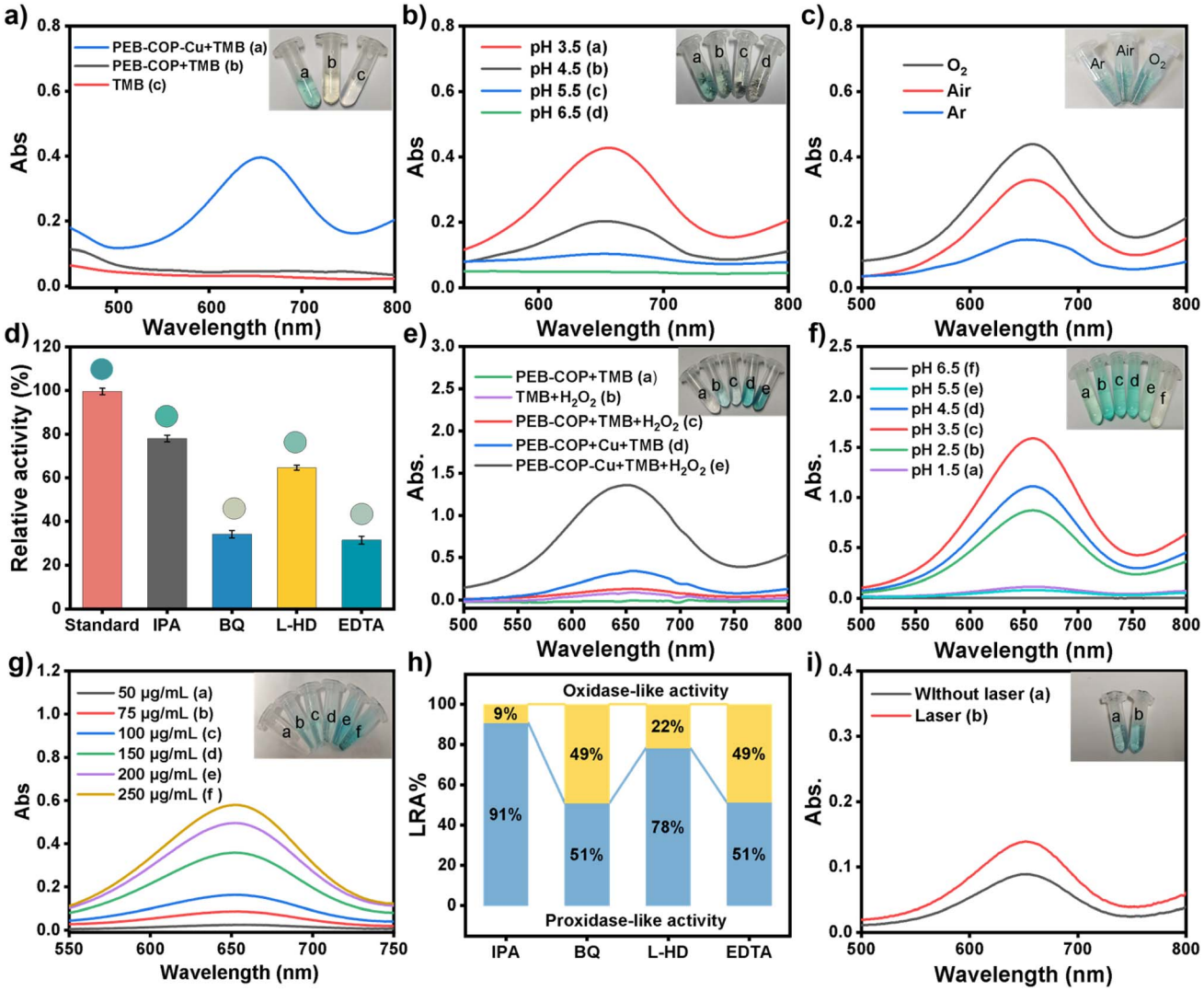

Fig. 4 OXD-like and POD-like activities of PEB-COP-Cu *in vitro* (Inset: Corresponding color change): (a) UV-visible absorption in different reaction systems at 652 nm; (b) UV-Vis absorption spectra of PEB-COP-Cu catalyzed TMB at different pH (250 μg mL^{-1}); (c) UV-Vis absorption spectra of PEB-COP-Cu-catalyzed TMB oxidation at 652 nm under saturated conditions of O_2, Air and Ar; (d) effect of different scavengers on the absorbance of the PEB-COP-Cu + TMB reaction system; (e) UV-visible absorption spectra of different systems with/without H_2O_2; (f) UV-Vis spectra of PEB-COP-Cu + H_2O_2 reaction system (250 μg mL^{-1}) at different pH; (g) UV-Vis spectra of PEB-COP-Cu + H_2O_2 system with different PEB-COP-Cu concentrations; (h) free radical validation analysis; (i) UV-Vis spectra of PEB-COP-Cu + TMB + H_2O_2 in the system at pH 5.5 with and without laser irradiation (250 μg mL^{-1}, 1.5 W cm^{-2}, 10 min).

originated from the synergistic interplay between the highly planar π-conjugated architecture and the bimetallic active sites, which collectively facilitated extensive electron delocalization within the framework, underscoring the strategic importance of metal-ion doping in optimizing photothermal therapy outcomes. The photothermal stability of PEB-COP-Cu was systematically evaluated through five cyclic laser irradiation experiments (Fig. 3f). As seen, PEB-COP-Cu exhibited exceptional thermal robustness, with negligible temperature fluctuations across all cycles, confirming its long-term operational reliability. The photothermal conversion efficiency (η) was quantified using eqn (S1)–(S3) based on a single heating–cooling cycle protocol.[44] As shown in Fig. 3g, the η value reached 42.6% ($R^2 = 0.994$, $\tau_s = 250$ s), surpassing many conventional POP-based photothermal agents (Table S1). To assess long-term aqueous stability, PEB-COP-Cu was stored in water for 14 days before photothermal testing (Fig. 3h). As seen, the temperature profiles remained identical to the initial measurements, demonstrating complete retention of photothermal activity and structural integrity. Meanwhile, PEB-COP-Cu dispersed in PBS at pH 7.4 demonstrated exceptional stability across dual testing protocols. UV-Vis spectra maintained precise overlap during 10 min exposure to 638 nm laser irradiation with measurements taken at 2 min intervals, confirming outstanding photostability (Fig. S7a). Concurrently, accelerated aging tests at 37 °C only showed slight absorbance variation after 30 days with measurements every 10 days, verifying long-term physiological stability (Fig. S7b). These results together validate its robustness

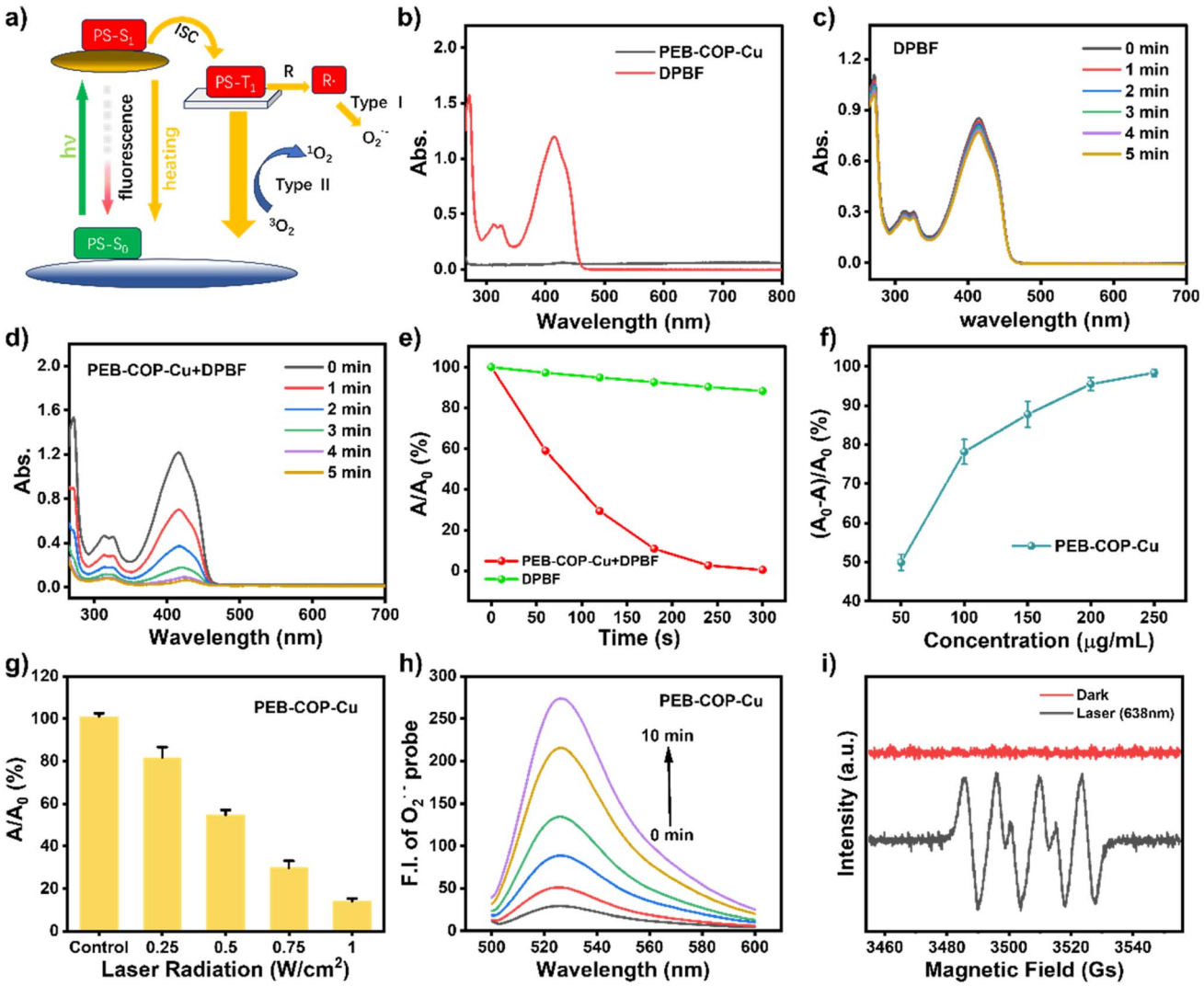

Fig. 5 Photodynamic testing of PEB-COP-Cu. (a) Schematic diagram of the photodynamic force generated by the photosensitizer; (b) UV-Vis absorption spectra of PEB-COP-Cu and TMB at 415 nm; (c) UV-Vis absorption change of DPBF after 5 minutes of laser irradiation (1.0 W cm^{-2}); (d) UV-Vis absorption changes of PEB-COP-Cu + DPBF under laser irradiation for 5 min (1.0 W cm^{-2}); (e) comparison of PEB-COP-Cu + DPBF and DPBF decay rates under laser irradiation (λ = 638 nm, 1.0 W cm^{-2}); (f) DFPB consumption after laser radiation for 5 min (1.0 W cm^{-2}) for different dispersion concentrations of PEB-COP-Cu. (g) DPBF decay rate induced by PEB-COP-Cu (250 μg mL^{-1}) at different laser powers; (h) fluorescence absorption spectra of $O_2^{\bullet-}$ capture by PEB-COP-Cu-induced dihydrorhodamine under laser illumination (250 μg mL^{-1}); (i) the EPR of PEB-COP-Cu detects O_2 in the dark or under laser irradiation (250 μg mL^{-1}, 1.0 W cm^{-2}, 638 nm).

for biomedical applications. Such superior stability demonstrated the great application potential of PEB-COP-Cu as a reusable and durable photothermal agent for antimicrobial therapy, where consistent heat generation was critical for bacterial eradication and wound healing.

Then, the mimicking enzyme activities of PEB-COP-Cu was evaluated. Initially, the oxidase-like (OXD) activity of PEB-COP-Cu was investigated *via* the chemical chromogenic method utilizing 3,3′,5,5′-tetramethylbenzidine (TMB) as a chromogenic substrate.[45] As illustrated in Fig. 4a, only in the media containing PEB-COP-Cu and TMB, simultaneously, obvious color change accompanied by distinctive UV absorption of oxTMB (652 nm), could be clearly observed. The PEB-COP-Cu displayed a pH-dependent enzyme activity progressively intensified with increasing acidity (Fig. 4b). Notably, PEB-COP-Cu also displayed a significant enzyme activity even at the acidity akin to the infectious microenvironment (pH = 5.5). Furthermore, the role of oxidizing agent (O_2) on the reaction system was also studied. As shown in Fig. 4c, the enzyme activity demonstrated a pronounced enhancement under oxygen-saturated conditions compared to argon (Ar)- or air-saturated media. However, the mimicking-OXD activity underwent a significant decline in an argon-filled environment. This observation suggested PEB-COP-Cu catalyzed the oxidation of TMB through the utilization of O_2 to produce reactive oxygen species (ROS).[46] To probe the ROS generated during the oxidation of TMB, we used 5 mM isopropanol (IPA), D-histidine (L-HD), *p*-benzoquinone (BQ), and ethylenediaminetetraacetic acid (EDTA), as trapping agents for

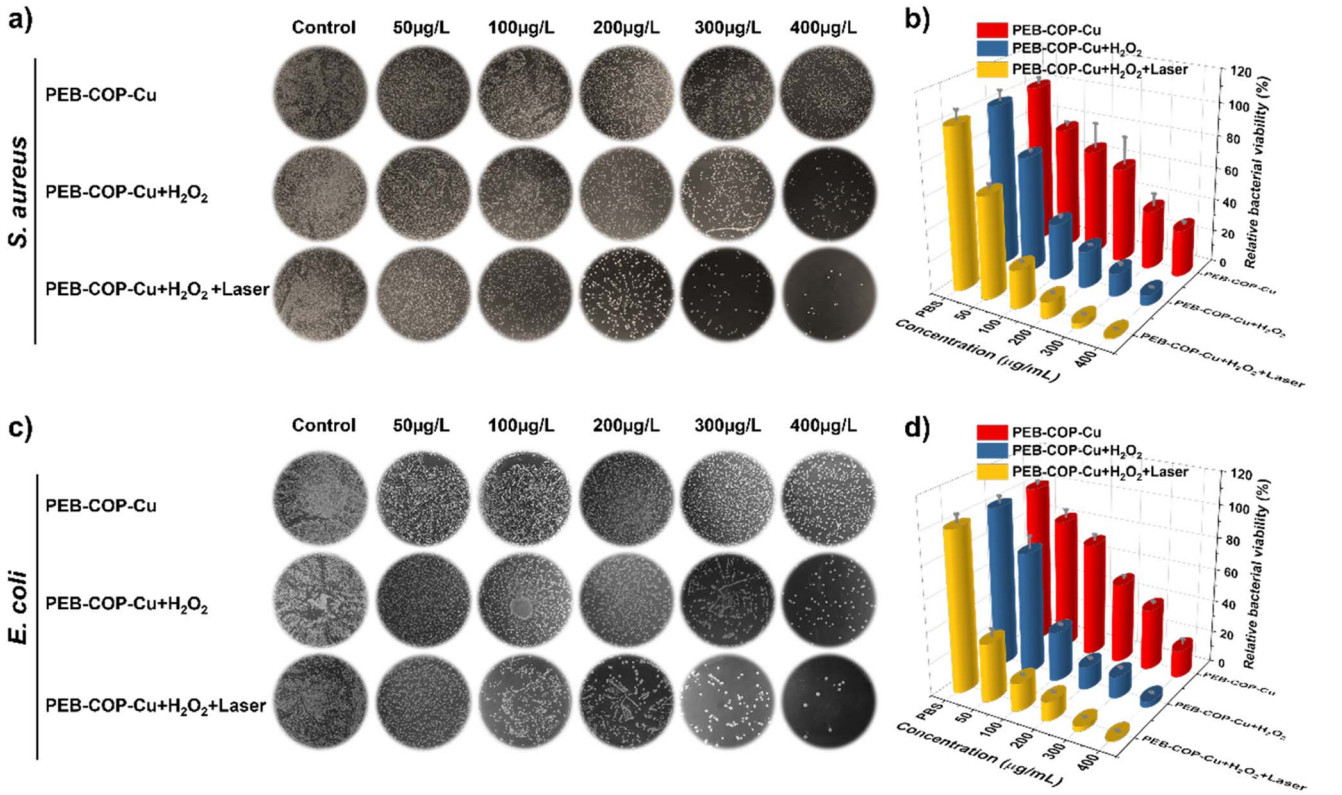

Fig. 6 (a) Pictures of colonies of *S. aureus* and (c) *E. coli* co-cultured with different concentrations of PEB-COP-Cu in the presence of H_2O_2 or in the co-presence of H_2O_2 and a 638 nm laser (1.0 W cm^{-2} for 10 min) for 24 h and treated; (b and d) corresponding cell viability graphs of *S. aureus* and *E. coli* determined by plate counting method, respectively. Results are presented as mean ± S.D. ($n = 3$, *$p < 0.05$, **$p < 0.01$, ***$p < 0.001$, ****$p < 0.0001$, analyzed by Student's *t*-test).

the hydroxyl radicals ($^{\bullet}OH$), singlet-linear oxygen ($^1O_2$), superoxide anion ($O_2^{\bullet-}$) and hole (h^+), respectively. As illustrated in Fig. 4d, compared with the minor decrease upon the addition of IPA and L-HD, the absorbance of the system exhibited a much substantial decline with the incorporation of BQ and EDTA. This consequence indicated the ROS produced by PEB-COP-Cu during the mimicking-OXD process were primarily $O_2^{\bullet-}$ and h^+, while $^{\bullet}OH$ and $^1O_2$ were generated in significantly smaller amounts. Based on these experimental results, it could be inferred that within the reaction system consisting of PEB-COP-Cu and TMB, dissolved oxygen (O_2) captured electrons transferred from PEB-COP-Cu, leading to its reduction to $O_2^{\bullet-}$ and the simultaneous formation of h^+. These species, in combination, significantly enhanced the catalytic efficiency of the direct oxidation of TMB, resulting in the formation of the color-developing product (oxTMB).[47] Thereby, even in the environment without H_2O_2, the as-prepared PEB-COP-Cu could also exert the antibacterial ability.

Meanwhile, the peroxidase-like (POD-like) activity of PEB-COP-Cu was also evaluated using TMB as a standard chromogenic substrate.[48] As presented in Fig. 4e, the characteristic absorbance at 652 nm for the PEB-COP-Cu + TMB + H_2O_2 system was higher than the PEB-COP-Cu + TMB system. This result revealed PEB-COP-Cu not only displayed oxidase-like (OXD-like) activity but primarily possesses significant POD-like activity, which could swiftly catalyze the decomposition of H_2O_2 to generate the highly oxidizing $^{\bullet}OH$, exhibiting POD-like activity. As illustrated in Fig. 4f, the mimicking activity of PEB-COP-Cu was also concerned with the media pH. Specifically, the POD-like activity first increased and then decreased with increasing acidity, which reached the maximal activity at the pH of 3.5. Notably, PEB-COP-Cu showed strong enzyme activity under acidity conditions comparable to the IME (pH 5.5). Furthermore, the oxidizing capability was proportional to the concentration of PEB-COP-Cu, which was progressively increased with rising concentration (Fig. 4g). Similarly, different ROS scavengers (IPA, L-HD, BQ and EDTA) were used to evaluate the POD-like catalytic mechanism of PEB-COP-Cu. The results in Fig. 4h showed the addition of IPA significantly reduced the absorbance of the PEB-COP-Cu + TMB + H_2O_2 group compared to the PEB-COP + TMB group, confirming the production of large amounts of $^{\bullet}OH$.[46] And the POD-like activity was further enhanced under laser illumination (Fig. 4i).[49] To elucidate the temperature-dependent enzymatic behavior, we systematically evaluated the POD-like and OXD-like activities of PEB-COP-Cu across a physiological to hyperthermal range (37–65 °C). Results demonstrated both the POD and OXD activities peaked at 45 °C, with enzymatic performance declining significantly above 55 °C (Fig. S8).

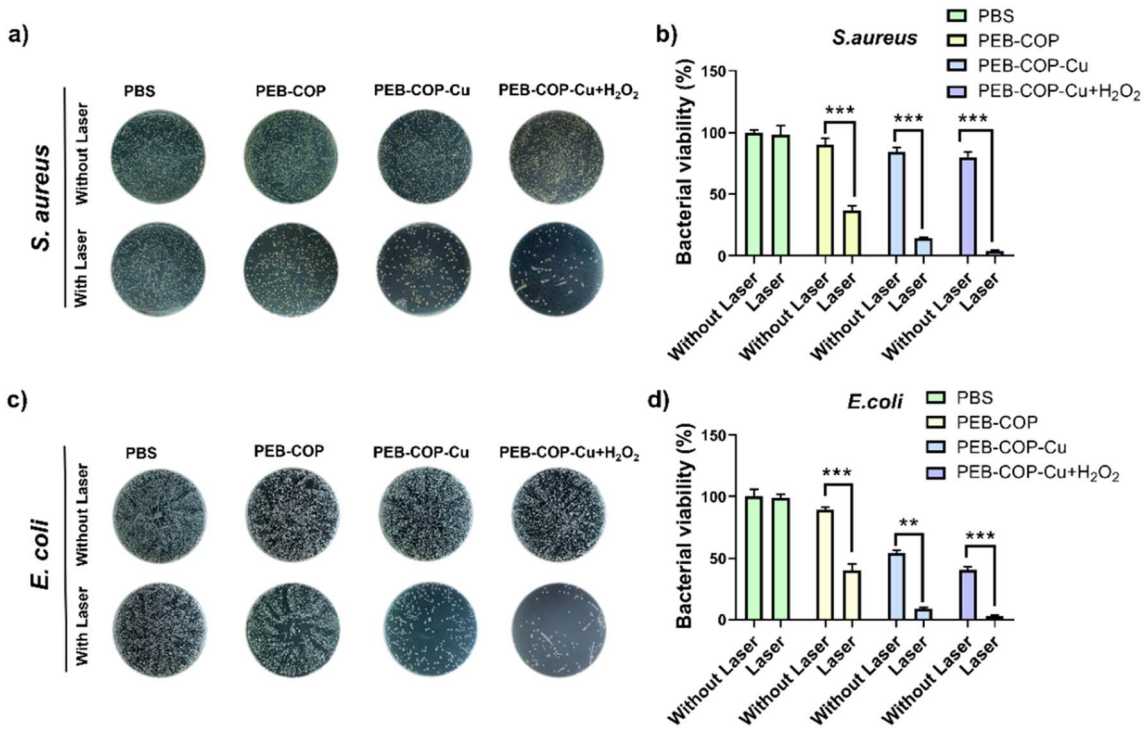

Fig. 7 (a) Pictures of colonies of *S. aureus* and (c) *E. coli* after co-culturing with different treatment conditions for 24 h with or without treatment by 638 nm laser (1.0 W cm^{-2}, 10 min). ($n = 3$) (b); (d) corresponding cell viability graphs of *S. aureus* and *E. coli* determined by plate counting method, respectively ($n = 3$).

As illustrated in Fig. 5a, upon laser irradiation (638 nm, 1.0 W cm^{-2}), photosensitive materials could dissipate energy through three primary pathways, including the fluorescence emission, vibrational relaxation (heat generation), and intersystem crossing (ISC), which generates triplet states and enhances reactive oxygen species (ROS) production.[50] To evaluate the PDT capacity of PEB-COP-Cu, we quantified ROS generation using 1,3-diphenylisobenzofuran (DPBF) as a singlet oxygen ($^1O_2$) probe and dihydrorhodamine (DHR) as a superoxide anion ($O_2^{\bullet-}$) indicator. As shown in Fig. 5b, the absorption of DPBF at 415 nm (characteristic of $^1O_2$ quenching) remained stable in the absence of PEB-COP-Cu. However, upon introducing PEB-COP-Cu and laser irradiation (Fig. 5c and d), the DPBF signal decreased by 99.62 ± 0.14% within 5 min, which was 8-fold higher than the control group (11.73 ± 0.62%, Fig. 5e). This result confirmed that PEB-COP-Cu efficiently converted molecular oxygen into $^1O_2$ *via* a Type II PDT mechanism.[51] As displayed in Fig. 5f and g, the Type II photodynamic activities of PEB-COP-Cu was positively correlated with both the sample concentration and the laser powers. Furthermore, as shown in Fig. 5h, a notable increase in fluorescence absorption by DHR was detected when exposed to laser. Additionally, as displayed in Fig. 5i, electron paramagnetic resonance (EPR) further confirmed the generation of $O_2^{\bullet-}$ under laser illumination.[52] This dual ROS-generating capability enabled PEB-COP-Cu to perform mixed Type I/II PDT, overcoming the limitations of hypoxia-associated treatment inefficiency. The integrated ROS-mediated pathways provided a synergistic antimicrobial strategy, effectively eradicating bacteria through oxidative stress while promoting wound healing.

Based on the exceptional photothermal, photodynamic and dual enzymatic activities, the *in vitro* antimicrobial activity of PEB-COP-Cu was assessed through the plate counting method, employing *Staphylococcus aureus* (*S. aureus*) and *Escherichia coli* (*E. coli*), as the representative strains of Gram-positive (G+) and Gram-negative (G−) bacteria (Fig. 6).[53] As seen from Fig. 6a and c, in stark contrast to the control group, the PEB-COP-Cu alone also presented obvious sterilizing activity ascribed to the intrinsic OXD-activity. Notably, upon the exertion of laser irradiation (638 nm, 1.0 W cm^{-2}, 10 min) and H_2O_2 (10 mmol L^{-1}), and the bactericidal ability of PEB-COP-Cu was prominently enhanced which also exhibited a concentration-dependent manner. Their bactericidal potential against both *S. aureus* (Fig. 6a) and *E. coli* (Fig. 6c) was significantly enhanced with increasing concentration. At a concentration of 50 μg mL^{-1}, only moderate bactericidal effect was observed in the PEB-COP-Cu group, with inhibition rates of 23.70 ± 1.56% and 17.65 ± 2.97% against *S. aureus* (Fig. 6b) and *E. coli* (Fig. 6d), respectively, assigned to the OXD-like enzyme activity. However, upon the addition of H_2O_2, the inhibitory effect of the PEB-COP-Cu + H_2O_2 group was increased to 27.75 ± 1.09% and 24.16 ± 4.53% against *S. aureus* (Fig. 6b) and *E. coli* (Fig. 6d), respectively, due to the catalysis of the OXD-like and POD-like enzymes. In contrast, the PEB-COP-Cu + H_2O_2 + laser group showed high inhibition towards both bacteria (36.46 ± 1.97% for *S. aureus* and 63.40 ± 2.92% for *E. coli*) attributed to the multiple

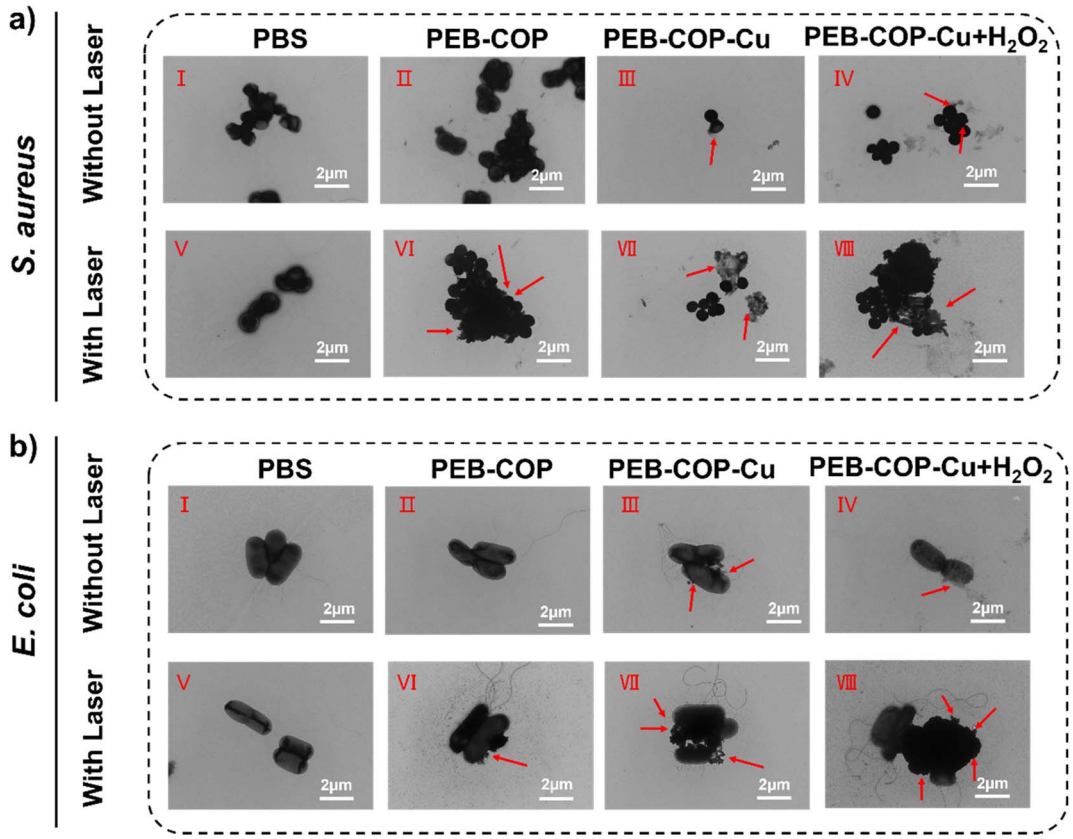

Fig. 8 TEM images of *S. aureus* (a) and *E. coli* (b) passing through (I) PBS, (II) POP, (III) PEB-COP-Cu, (IV) PEB-TEM images of *S. aureus* (a) and *E. coli* (b) passing through (I) PBS, (II) POP, (III) PEB-COP-Cu, (IV) PEB-COP-Cu + H_2O_2, (V) PBS + laser, (VI) POP + laser, (VII) PEB-COP-Cu + laser and (VIII) PEB-COP-Cu + H_2O_2 + laser. The red tip in the image represents the location of the injury. (Concentration: 250 μg mL^{-1}; laser radiation = 1.0 W cm^{-2}; scale bar = 2 μm; radiation emission time = 10 min); (e) crystalline violet staining results of *S. aureus* and *E. coli* after exposure to different treatments; (f); (g) OD quantification of crystal violet staining results of *Staphylococcus aureus* and *Escherichia coli* after exposure to different treatments.

therapies. With the concentration of 400 μg mL^{-1}, PEB-COP-Cu alone achieved significant inhibition against both pathogens with 82.75 ± 1.99% and 70.66 ± 1.18% for *E. coli* and *S. aureus*, respectively. The PEB-COP-Cu + H_2O_2 combination markedly enhanced efficacy, exceeding 90% inhibition for both stains (96.30 ± 0.49% and 93.69 ± 0.34% for *E. coli* and *S. aureus*). Near-total eradication was observed with PEB-COP-Cu + H_2O_2 + laser treatment at the sample concentration of 300 μg mL^{-1} (99.17 ± 0.21%, and 97.31 ± 0.01% for *E. coli* and *S. aureus*). To assess the therapeutic efficacy of PTT, *S. aureus* and *E. coli* were separately co-cultured with PEB-COP-Cu across a concentration gradient (0–300 μg mL^{-1}). To isolate photothermal effects from photodynamic contributions, ROS scavengers were introduced during bacterial co-culture. Following exposure to laser irradiation, bactericidal efficacy was quantified *via* plate counting. Results demonstrated dose-dependent thermal killing, with bacterial viability at the maximum concentration (300 μg mL^{-1}) reduced to 24.50 ± 1.06% for *S. aureus* and 26.30 ± 1.17% for *E. coli.*

Furthermore, recognizing the urgent need for new antimicrobials against difficult-to-treat pathogens, we selected *Pseudomonas aeruginosa* (*P. aeruginosa*), a clinically critical multidrug-resistant bacterium, as a model to rigorously assess the antimicrobial efficacy of PEB-COP-Cu against challenging targets. After co-culture across a concentration gradient (0–300 μg mL^{-1}), PEB-COP-Cu treatment exhibited a robust, dose-dependent bactericidal effect. Critically, this culminated in near-complete bacterial eradication, with survival plummeting to a mere 12.24 ± 0.42% at the highest concentration tested (300 μg mL^{-1}, Fig. S10). This potent efficacy unequivocally demonstrated not only the intrinsic bactericidal capacity of PEB-COP-Cu, but also strongly suggested its ability to effectively bypass the common resistance mechanisms of this problematic pathogen. Consequently, PEB-COP-Cu represented a highly promising candidate for combating drug-resistant bacterial strains.

To elucidate the sterilization mechanism and optimize therapeutic strategies, *S. aureus* and *E. coli* were subjected to eight distinct treatments (250 μg mL^{-1}), including the PBS control, PBS + laser, PEB-COP, PEB-COP + laser, PEB-COP-Cu, PEB-COP-Cu + laser, PEB-COP-Cu + H_2O_2, and PEB-COP-Cu + H_2O_2 + laser. Fig. 7 demonstrated bacterial viability after 12 h incubation across these experimental groups. As depicted in Fig. 7a and c, the bacterial colonies in the PBS groups exhibited

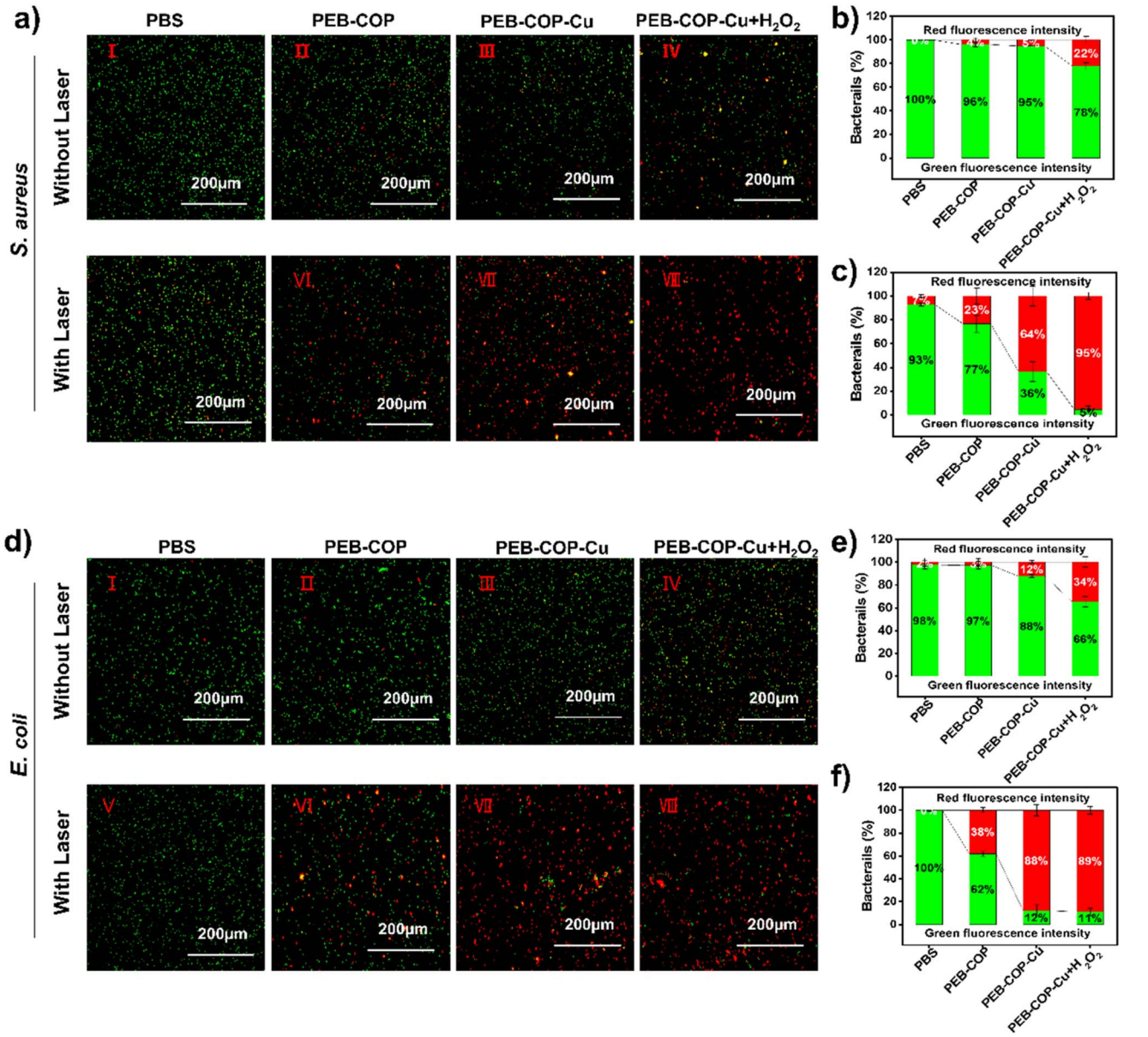

Fig. 9 *S. aureus* (a) and *E. coli* (d) PI and SYTO 9 co-staining by (I) PBS, (II) PEB-COP, (III) PEB-COP-Cu, (IV) PEB-COP-Cu + H_2O_2, (V) PBS + laser, (VI) PEB-COP + laser, (VII) PEB-COP-Cu + laser, and (VIII) PEB-COP-Cu + H_2O_2 + laser Fluorescence images (concentration: 250 μg mL^{-1}; laser = 1.5 W cm^{-2} for 10 min; scale bar = 200 μm); (b) and (e) Fluorescence intensity analysis of PBS, PEB-COP,PEB-COP-Cu and PEB-COP + H_2O_2 in without laser treatment for *S. aureus* and *E. coli*, respectively; (c) and (f) fluorescence intensity analysis of PBS, PEB-COP,PEB-COP-Cu and PEB-COP + H_2O_2 after laser treatment for *S. aureus* and *E. coli*, respectively.

comparable numbers regardless of the laser irradiation. However, the antimicrobial efficacy of PEB-COP, PEB-COP-Cu, and PEB-COP-Cu + H_2O_2 was notably enhanced after the laser irradiation, especially the PEB-COP-Cu + H_2O_2. Specifically, the PEB-COP + laser group demonstrated 63.31 ± 2.23% and 59.71 ± 2.59% antimicrobial activity against *S. aureus* and *E. coli*, respectively, much high than that in the laser free conditions (9.72 ± 2.34% and 10.71 ± 0.91%). In contrast, the PEB-COP-Cu + laser group showed 85.73 ± 0.61% and 91.2 ± 0.77% inhibition against *S. aureus* and *E. coli*, respectively, much higher than these in the laser free conditions (15.42 ± 1.65% and 45.62 ± 1.09%). Notably, the inhibition of *S. aureus* and *E. coli* in the PEB-COP-Cu + H_2O_2 group soared to 95.80 ± 0.31% and 96.78 ± 0.26%, respectively, after laser radiation (Fig. 7b and d). Among all treatments, the PEB-COP-Cu + H_2O_2 group demonstrated the most pronounced antimicrobial effect, attributed to the synergistic photodynamic-photothermal and dual enzyme antimicrobial properties of PEB-COP-Cu.

TEM revealed distinct morphological alterations in *S. aureus* and *E. coli* following PEB-COP-Cu treatments. As shown in Fig. 8a and b, bacterial cells in PBS control and PBS + laser groups maintained structural integrity with intact cell walls and membranes. Conversely, laser-activated treatment groups (POP + laser, PEB-COP-Cu + laser, and PEB-COP-Cu + H_2O_2 + laser)

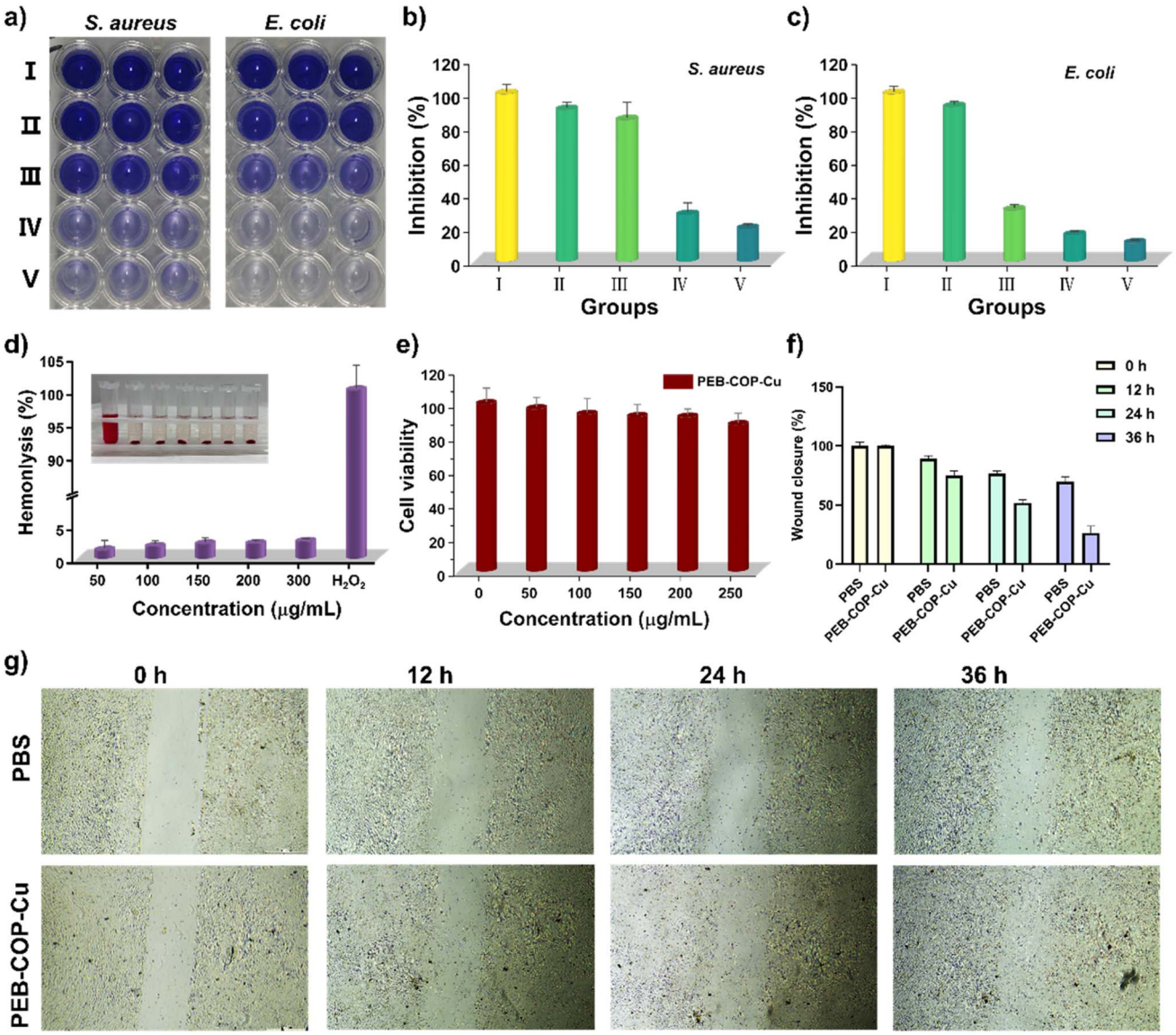

Fig. 10 (a) Crystalline violet staining results of *S. aureus* and *E. coli* after the (I) PBS, (II) PEB-COP, (III) PEB-COP-Cu, (IV) PEB-COP-Cu + Laser, and (V) PEB-COP-Cu + H_2O_2 + laser treatments; (b and c) OD quantification of crystal violet staining results of *S. aureus* and *E. coli* after exposure to different treatments; (d) effect of the concentration of PEB-COP-Cu on the hemolysis rate; (e) effect of the concentration of PEB-COP-Cu on the viability of 3T3 cells; (f) statistical analysis of (g); (g) effect of PEB-COP-Cu on the migration of cells at the working concentrations.

exhibited substantial cellular damage. Most notably, the PEB-COP-Cu + H_2O_2 + laser group demonstrated severe membrane disintegration and cytoplasmic leakage, significantly exceeding damage observed in other groups. These findings confirmed the synergistic bactericidal mechanism combining photothermal/photocatalytic properties of PEB-COP-Cu with enzymatic activities.[54]

Bacterial viability was quantified using SYTO9/PI dual-staining (Fig. 9). As seen, the control groups (PBS with/without laser) exhibited exclusive green fluorescence. Conversely, laser-activated treatments (PEB-COP-Cu + laser; PEB-COP-Cu + H_2O_2 + laser) showed dominant red fluorescence (Fig. 9c–f), with maximal intensity in the PEB-COP-Cu + H_2O_2 + laser group, aligning with TEM observations of severe cellular damage. Quantitative analysis revealed the PEB-COP-Cu alone induced minimal death, as verified by the weak red fluorescence (<5%), due to mimicking-OXD activity. However, the addition of external stimuli (Laser irradiation or the H_2O_2) triggered robust ROS generation, especially the concurrently exertion of laser and H_2O_2 (>90% red fluorescence). This dual staining strategy corroborated the TEM findings and demonstrated the multi-modal antimicrobial efficacy of PEB-COP-Cu through combined PDT, PTT, and dual enzymatic pathways.

Building on its exceptional antimicrobial properties, the biofilm inhibition efficacy of PEB-COP-Cu was evaluated *via* Crystal violet (CV) assay.[55] Stereomicroscopy (Fig. 10a) revealed substantial residual biofilms in PEB-COP-Cu-only groups (without activation). Significant degradation occurred upon

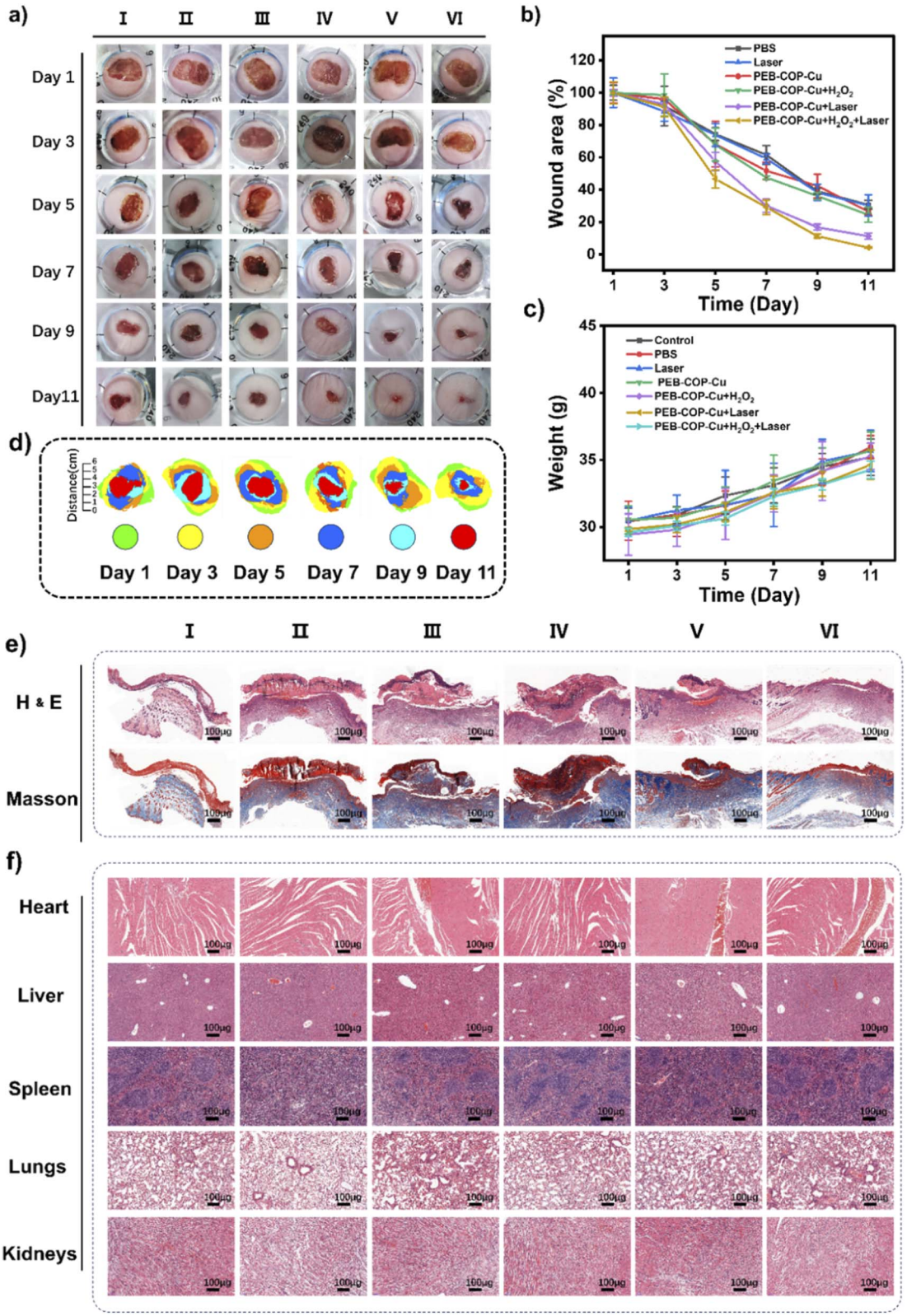

Fig. 11 (a) Images of wounds on days 1, 3, 5, 7, 9, and 11 in different treatment groups; (b) quantitative analysis of wound area in varied groups; (c) changes in body weight of mice in different groups; (c) simulation results of wound traces of regenerated skin; (d) visualization of wound healing in mice during the treatment process; (e) histological analysis of regenerated skin tissues at the wound site by H&E staining and Masson trichrome staining on day 11, scale bar = 100 μm; (f) H&E staining on the major organs of mice following various treatments.

activation (laser or H_2O_2), with maximal biofilm clearance observed under combined PEB-COP-Cu + H_2O_2 + laser treatment. Crystal violet quantification (Fig. 10b and c) confirmed the advantage of PEB-COP-Cu + H_2O_2 + laser treatment with synergistic inhibition efficacy of 80.54 ± 0.82% and 89.02 ± 0.21% for *S. aureus* and *E. coli*. In contrast, the PEB-COP-Cu alone exhibited limited activity (9.48 ± 1.76% against *S. aureus* and 7.72 ± 1.06% against *E. coli*). Notably, PEB-COP-Cu maintained significant inhibition activity under the laser irradiation. The PEB-COP-Cu + H_2O_2, achieved 69.50 ± 1.06% and 15.48 ± 5.19% biofilm inhibition for *E. coli* and *S. aureus*. These results not only corroborated our earlier antimicrobial assessments, but also elucidated the unique dual-action mechanism of PEB-COP-Cu.

To assess the translational potential of PEB-COP-Cu, the *in vitro* biosafety was evaluated.

Initial hemocompatibility assessment *via* standardized erythrocyte hemolysis assay revealed a dose-dependent increase in hemolysis rate with PEB-COP-Cu concentration (Fig. 10d, and S6a). Crucially, despite this trend, hemolysis remained exceptionally low (<5%) across the entire therapeutic concentration range (0–600 μg mL^{-1}), reaching only 2.56 ± 0.08% at the concentration of (300 μg mL^{-1}) and a negligible 3.57 ± 1.08% even at 600 μg mL^{-1}.[56] This demonstrates outstanding blood compatibility and minimal erythrocyte membrane disruption.[57]

Complementing this, *in vitro* cytotoxicity assessment using mouse fibroblast (3T3) cells (Fig. 10e and S6b) showed consistently high cell viability (>80%) across all concentrations (0–600 μg mL^{-1}). Critically, viability was maintained at >80% even at 300 μg mL^{-1} (optimal dose) and 600 μg mL^{-1} (maximum dose), confirming low cytotoxicity within the biologically relevant range. These collective findings robustly establish the favorable biocompatibility profile of PEB-COP-Cu at its effective antimicrobial concentrations.

Furthermore, scratch wound healing assays were performed to evaluate the capacity of PEB-COP-Cu in modulating regenerative processes. Time-lapse imaging quantified progressive wound closure, revealing significant acceleration of cellular restitution mechanisms compared to controls (Fig. 10f–g). Both PBS control and PEB-COP-Cu groups showed progressive wound closure from 0–36 h. Significantly, PEB-COP-Cu treatment accelerated cell migration, achieving 73.54 ± 3.28% closure at 36 h *versus* 26.46 ± 2.68% in controls. This time-dependent enhancement demonstrates the capacity of PEB-COP-Cu to stimulate reparative processes.[58] In conclusion, PEB-COP-Cu leverages the divergent pathophysiological conditions, particularly the pH gradient and ROS homeostasis, between the infected microenvironment (acidic pH, ROS amplification susceptibility, stressed antioxidants) and normal tissue (neutral pH, robust antioxidant capacity) to achieve selective bacterial eradication. Critically, the controlled, context-dependent release of essential copper ions at the wound site also contributes positively to tissue regeneration through established pro-healing biological pathways.

The *in vivo* assay was finely evaluated utilizing a *S. aureus*-infected dorsal wound model in KM rats. All animal experiments adhered strictly to the animal experimentation guidelines of Shandong Second Medical University.[59] The rats were divided into six groups, including the PBS (I), PEB-COP-Cu (II), laser (III), PEB-COP-Cu + H_2O_2 (IV), PEB-COP-Cu + laser (V), and PEB-COP-Cu + H_2O_2 + laser (VI). On the initial day of treatment, all groups exhibited pus and redness due to bacterial infection, with wounds visibly stretched and deformed, confirming the successful establishment of the infected wound model. As seen from Fig. 11a, the wounds in all these therapeutic groups were gradually decreased with the duration of time, but varied degrees of healing were detected in different groups. Quantitative tracking of wound closure (Fig. 11b, and d) revealed accelerated healing in laser-activated groups, particularly the PEB-COP-Cu + H_2O_2 + laser group. Notably, Group VI exhibited the most pronounced wound healing enhancement, demonstrating synergistic therapeutic efficacy in infected wound repair. Specifically, by the 5th day post-infection, the wounds began to contract in the PEB-COP-Cu + H_2O_2 + laser as the decrease of wound area decreased to 46.62 ± 3.31% (*vs.* 57.42 ± 3.29% of PEB-COP-Cu + laser, 67.81 ± 5.84% of PEB-COP-Cu + H_2O_2, 73.87 ± 4.13% of PBS + laser, 68.11 ± 8.14% of PEB-COP-Cu, and 73.39 ± 2.31% of PBS). On day 11, the PEB-COP-Cu + H_2O_2 + laser (VI) group achieved a wound healing rate of 95.82 ± 0.30%, outperforming the other groups (88.72 ± 1.15%, 75.63 ± 2.69%, 69.84 ± 3.90% 3.51 ± 1.32%, and 69.40 ± 1.60% for the PEB-COP-Cu + laser, PEB-COP-Cu + H_2O_2, PBS + laser, PEB-COP-Cu, and PBS, respectively). These consequences showed the great efficacy of PEB-COP-Cu + H_2O_2 + laser in bacterial eradication and wound healing, facilitated by the synergistic action of enzyme catalysis and photo therapy. Furthermore, as presented in Fig. 11c, similar to the PBS group, the body weights of mice in various treatment groups was all increased stable during the 11 days treatment with no intensive fluctuation. Histopathological assessment *via* hematoxylin-eosin (H&E) and Masson trichrome staining revealed advanced tissue regeneration in Group VI, characterized by complete epidermal reconstruction, robust neovascularization and minimal inflammatory infiltrate (Fig. 11e). This regenerative profile demonstrated significant bacterial clearance coupled with accelerated wound contraction of PEB-COP-Cu. The combinatorial photo-enzymatic strategy outperformed monotherapies through synergistic tissue remodeling. The systemic biocompatibility of PEB-COP-Cu was further evaluated through comprehensive hematological and histopathological analyses. On day 11, orbital venous plexus blood samples collected from all groups (Fig. S5) revealed no statistically significant alterations in hematological parameters compared to controls, confirming systemic hemocompatibility. Furthermore, histological examination using H&E staining of all major organs of the mice revealed no significant tissue damage, indicating that PEB-COP-Cu exhibited excellent biosafety and did not elicit any notable adverse effects on the tissues and organs (Fig. 11f).[60]

Conclusion

In this study, we engineered a photoactive copper-coordinated covalent organic polymer (PEB-COP-Cu) *via* a green, cost-

effective Michael addition–elimination strategy. This multifunctional platform integrated dual enzyme-mimicking activities (OXD/POD-like) with photothermal and photodynamic capabilities, establishing a synergistic approach for infected wound therapy. The intrinsic photodynamic/thermal properties of PEB-COP-Cu induce photo-enhanced catalytic activity, enabling simultaneous bacterial and biofilm eradication through PTT-mediated thermal ablation, multi-ROS cascades. Critically, PEB-COP-Cu operates through dual mechanisms, in which the hybrid Type I/II photodynamic pathways mitigated oxygen dependency and the oxidase/peroxidase–mimetic activity generating $^{\bullet}OH$. This concerted action overcome fundamental limitations in wound therapy, oxygen scarcity and hydrogen peroxide insufficiency, while maximizing reactive species diversity. PEB-COP-Cu represented a paradigm-shifting therapeutic agent that coordinates rapid sterilization, biofilm penetration and pro-regenerative activity. Leveraging sustainable synthesis and multimodal bactericidal action, this work establishes a blueprint for next-generation infected wound therapeutic agent.

Author contributions

Chunzhen Zhao, Writing–original draft. Changxiao Du, Formal analysis. Jie Xu, Funding acquisition. Yuqing Zhao, Investigation methodology. Xiaoming Shi, Investigation methodology. Dong Zhang, Investigation methodology. Xinmiao Zhang, Conceptualization data curation. Yi Zhang, Resources. Han Sun, Resources. Xixin Jiang, Software. Zhen Du, Software, Mengjin Wang, Software. Meimei Xiao, Project administration. Mingwen Zan, Supervision validation and visualization.

Conflicts of interest

The authors declare there are no conflicts of interest. All animal procedures were performed in accordance with the Guidelines for Care and Use of Laboratory Animals of Shandong Second Medical University and approved by the Animal Ethics Committee of Shandong Second Medical University.

Data availability

Data will be made available on request.

The SI includes a comprehensive list of all chemicals, solvents, and biological materials used, along with their sources and purity levels; experimental procedures; characterization data such as ^{1}H-NMR spectra, N_2 adsorption isotherms, pore size distribution curves, and EDS spectra; optical properties including UV-visible spectra and corresponding calibration curves; assessments of light and water stability; temperature-dependent POD and OXD mimetic activities; studies on photothermal antibacterial efficacy; biocompatibility evaluations; *in vivo* blood test results from mouse models; supplementary tables; and a full set of supporting references. See DOI: **https://doi.org/10.1039/d5ra04493f**.

Acknowledgements

This work was supported by funding from Natural Science Foundation of Shandong Province (ZR2020QB067), Shandong Second Medical University Public Sent Domestic Study and Visiting Project (20237-21), Science and Technology Project of Traditional Chinese Medicine of Shandong Province (M-2022055), Traditional Chinese Medicine Research Project of Weifang Health Commission (WFZYY2022-03-013) and Weifang Youth Medical Talent Lifting Project.

References

1 F. Shirkhan, F. Safaei, S. Mirdamadi and M. Zandi, The Role of Probiotics in Skin Care: Advances, Challenges, and Future Needs, *Probiotics Antimicrob. Proteins*, 2024, **16**, 2132–2149.
2 L. Fialho, J. Albuquerque, A. S. Pinho, A. M. Pereira, C. Monteiro, N. Oliveira, S. Ferreira and M. C. L. Martins, Exploring innovative adhesive approaches to manage medical adhesive-related skin injuries (MARSI), *Int. J. Adhes. Adhes.*, 2024, **130**, 103636.
3 Z. Chen, X. Zhao, L. Lin, Y. Cui, D. Cao, X.-L. Chen and X. Wang, CaGA nanozymes with multienzyme activity realize multifunctional repair of acute wounds by alleviating oxidative stress and inhibiting cell apoptosis, *Biomater. Sci.*, 2025, 422–433.
4 A. Sharma, N. Jangra, D. Dheer, S. K. Jha, G. Gupta, V. Puri and P. Kesharwani, Understanding the journey of biopolymeric nanoformulations for oral drug delivery: Conventional to advanced treatment approaches, *Eur. Polym. J.*, 2024, **218**, 113338.
5 A. Mutlu, E. J. Vanderpool, K. P. Rumbaugh, S. P. Diggle and A. S. Griffin, Exploiting cooperative pathogen behaviour for enhanced antibiotic potency: A Trojan horse approach, *Microbiology*, 2024, **170**, 001454.
6 G. Wu, Z. Xu, Y. Yu, M. Zhang, S. Wang, S. Duan and X. Liu, Biomaterials-based phototherapy for bacterial infections, *Front. Pharmacol*, 2024, **15**, 1513850.
7 L. Song and J. Li, Ultrasensitive NIR-II Surface-Enhanced Resonance Raman Scattering Nanoprobes with Nonlinear Photothermal Effect for Optimized Phototheranostics, *Small*, 2025, **21**, 2407787.
8 K. Zhu, S. Qian, H. Guo, Q. Wang, X. Chu, X. Wang, S. Lu, Y. Peng, Y. Guo, Z. Zhu, T. Qin, B. Liu, Y.-W. Yang and B. Wang, pH-Activatable Organic Nanoparticles for Efficient Low-Temperature Photothermal Therapy of Ocular Bacterial Infection, *ACS Nano*, 2022, **16**, 11136–11151.
9 K. Wang, X. Wang, L. Zhang, Y. Tang, J. Zhao, Y. Feng, R. Gao, Y. Hao and X. Tang, Coordination-Driven *in Situ* Grown Copper Peroxide in Mesoporous Dopamine with Self-Supplied H2O2 for Synergistic Enhanced PTT/CDT Antibacterial Treatment and Wound Healing, *ACS Appl. Mater. Interfaces*, 2024, **16**, 64579–64591.
10 Y. Wu, J. Li, L. Zhu, D. Wang, J. Song, X. Yu, Y. Li and B. Z. Tang, Photosensitive AIEgens sensitize bacteria to oxidative damage and modulate the inflammatory

responses of macrophages to salvage the photodynamic therapy against MRSA, *Biomaterials*, 2024, **309**, 122583.

11 Y. Yang, T. Hu, K. Zhao, Y.-C. Wang, Y. Zhu, S. Wang, Z. Zhou, L. Gu, C. Tan and R. Liang, Metal Doping Enabling Defective CoMo-Layered Double Hydroxide Nanosheets as Highly Efficient Photosensitizers for NIR-II Photodynamic Cancer Therapy, *Adv. Mater.*, 2025, **37**, 2405847.

12 W. Wang, Z. Li, C. Liu, H. Yu and Y. Sun, Application of Drug Delivery System Based on Nanozyme Cascade Technology in Chronic Wound, *Adv. Healthcare Mater.*, 2024, **13**, 2402559.

13 Y. An, X. Fang, J. Cheng, S. Yang, Z. Chen and Y. Tong, Research progress of metal–organic framework nanozymes in bacterial sensing, detection, and treatment, *RSC Med. Chem.*, 2024, **15**, 380–398.

14 R. Zhang, X. Yan and K. Fan, Nanozymes Inspired by Natural Enzymes, *Acc. Mater. Res.*, 2021, **2**, 534–547.

15 Y. Li, W. Ma, J. Sun, M. Lin, Y. Niu, X. Yang and Y. Xu, Electrochemical generation of Fe3C/N-doped graphitic carbon nanozyme for efficient wound healing in vivo, *Carbon*, 2020, **159**, 149–160.

16 Y. Li, L. Zhao, M. Liu, X. Zeng, Y. Zhao and B. Zhou, Multifunctional Polyoxovanadate-Based Covalent Organic Polymer for Bacteria-Infected Wound Therapy, *ACS Appl. Nano Mater.*, 2024, **7**, 26928–26940.

17 F. Zhao, H. Yu, C. Wang, J. Xu, H. Gao, Y. Ying, W. Li, J. Li, J. Zheng, L. Qiao, S. Che and J. Yu, Copper/iron bimetal phenolic networks boosted apoptosis/ferroptosis/cuproptosis combined tumor therapy through dual glutathione depletion, *Chem. Eng. J.*, 2024, **500**, 157408.

18 X. Zhang, Y. Min, Q. Zhang, S. Wu, W. Fu, J. Wu, M. Li, Y. Wang and P. Zhang, Functionalized Mn3O4 Nanosheets with Photothermal, Photodynamic, and Oxidase-Like Activities Triggered by Low-Powered Near-Infrared Light for Synergetic Combating Multidrug-Resistant Bacterial Infections, *Adv. Healthcare Mater.*, 2022, **11**, 2200121.

19 Z. Yu, T. Liu, X. Zheng, Y. Wang, J. Sha, L. Shan, T. Mu, W. Zhang, C. S. Lee, W. Liu and P. Wang, A glutathione responsive photosensitizer based on hypocrellin B for photodynamic therapy, *Spectrochim. Acta, Part A*, 2025, **325**, 125052.

20 S. Manole, D.-H. Nguyen, J.-J. Min, S. Zhou and N. Forbes, Setting "cold" tumors on fire: Cancer therapy with live tumor-targeting bacteria, *Med*, 2024, 100549.

21 B.-H. Han, Porous organic polymers, *J. Polym. Sci.*, 2024, **62**, 1491–1492.

22 Y. Zhang, X. Deng, L. Xia, J. Liang, M. Chen, X. Xu, W. Chen, J. Ding, C. Yu, L. Liu, Y. Xiang, Y. Lin, F. Duan, W. Feng, Y. Chen and X. Gao, Living Therapeutics for Synergistic Hydrogen-Photothermal Cancer Treatment by Photosynthetic Bacteria, *Adv. Sci.*, 2025, **12**, 2408807.

23 A. E. Eichstadt, T. C. Ward, M. D. Bagwell, I. V. Farr, D. L. Dunson and J. E. McGrath, Structure-property relationships for a series of amorphous partially aliphatic polyimides, *J. Polym. Sci., Part B:Polym. Phys.*, 2002, **40**, 1503–1512.

24 J. Yuan, J. Yu, L. Ma, Y. Ma, H. Hao, C. Zhao and B. Zhou, Michael addition-elimination reaction derived covalent organic polyrotaxane xerogels for ultra-high-efficiency capture of iodine pollutants, *J. Environ. Chem. Eng.*, 2024, **12**, 114531.

25 Y. Liu, Y. Wang, H. Li, X. Guan, L. Zhu, M. Xue, Y. Yan, V. Valtchev, S. Qiu and Q. Fang, Ambient aqueous-phase synthesis of covalent organic frameworks for degradation of organic pollutants, *Chem. Sci.*, 2019, **10**, 10815–10820.

26 H. Li, C. Huang, Y. Li, W. Yang and F. Liu, Electrocatalytic reduction of trace nitrobenzene using a graphene-oxide@polymerized-manganese-porphyrin composite, *RSC Adv.*, 2019, **9**, 22523–22530.

27 S. Belali, A. R. Karimi and M. Hadizadeh, Cell-specific and pH-sensitive nanostructure hydrogel based on chitosan as a photosensitizer carrier for selective photodynamic therapy, *Int. J. Biol. Macromol.*, 2018, **110**, 437–448.

28 G. Prabhavathi, M. Arjun and R. Yamuna, Synthesis, characterization and photoluminescence properties of tetra(aminophenyl) porphyrin covalently linked to multi-walled carbon nanotubes, *J. Chem. Sci.*, 2017, **129**, 699–706.

29 C. Liu, X.-D. Zhang, J.-M. Huang, M.-X. Guan, M. Xu and Z.-Y. Gu, In Situ Reconstruction of Cu–N Coordinated MOFs to Generate Dispersive Cu/Cu2O Nanoclusters for Selective Electroreduction of CO2 to C2H4, *ACS Catal.*, 2022, **12**, 15230–15240.

30 M. Kaur, Imine-Decorated Copper-Based Metal-Organic Framework for the Photodegradation of Methylene Blue, *J. Fluoresc.*, 2024, **34**, 1119–1129.

31 M. R. Rao, Y. Fang, S. De Feyter and D. F. Perepichka, Conjugated Covalent Organic Frameworks *via* Michael Addition–Elimination, *J. Am. Chem. Soc.*, 2017, **139**, 2421–2427.

32 X. Guan, Y. Qian, X. Zhang and H.-L. Jiang, Enaminone-Linked Covalent Organic Frameworks for Boosting Photocatalytic Hydrogen Production, *Angew. Chem., Int. Ed.*, 2023, **62**, e202306135.

33 D. Luo, H. Zhao, F. Liu, H. Xu, X. Dong, B. Ding, H. Dou and X. Zhang, Outstanding Lithium Storage Performance of a Copper-Coordinated Metal-Covalent Organic Framework as Anode Material for Lithium-Ion Batteries, *Energy Environ. Mater.*, 2024, **7**, e12732.

34 Z.-D. Ding, W. Zhu, T. Li, R. Shen, Y. Li, Z. Li, X. Ren and Z.-G. Gu, A metalloporphyrin-based porous organic polymer as an efficient catalyst for the catalytic oxidation of olefins and arylalkanes, *Dalton Trans.*, 2017, **46**, 11372–11379.

35 F. Chu, G. Hai, D. Zhao, S. Liu, Y. Hu, G. Zhao, B. Peng, G. Wang and X. Huang, Regulating Keto–Enol Tautomerism of β-Ketoenamine Covalent–Organic Frameworks for Photocatalytic Oxidative Coupling of Amines, *ACS Catal.*, 2023, **13**, 13167–13180.

36 B. Gao, B. Tan, Y. Liu, C. Wang, Y. He and Y. Huang, A study of FTIR and XPS analysis of alkaline-based cleaning agent for removing Cu-BTA residue on Cu wafer, *Surf. Interface Anal.*, 2019, **51**, 566–575.

37 J. Shao, X. Liang, Y. Lin, S. Wang, Z. Deng, G. Meng and X. Fang, KrF excimer laser induced damage and its mechanism of CaF2 single crystal with (111), (110) and (100) planes, *Appl. Surf. Sci.*, 2022, **586**, 152716.
38 Z. Wu, X. Huang, X. Li, G. Hai, B. Li and G. Wang, Covalent-organic frameworks with keto-enol tautomerism for efficient photocatalytic oxidative coupling of amines to imines under visible light, *Sci. China:Chem.*, 2021, **64**, 2169–2179.
39 Z. Bohström and K. P. Lillerud, Preparation of chabazite with mesopores templated from a cationic polymer, *Microporous Mesoporous Mater.*, 2018, **271**, 295–300.
40 Y. Hu, G. Liu, T. Song, X. Hu, B. Long and G.-J. Deng, Single-atom Cu sites on covalent organic frameworks with Kagome lattices for visible-light-driven CO2 reduction to propylene, *Appl. Catal. B Environ.*, 2025, **361**, 124587.
41 A. P. Veedu, B. Jeyakumar, A. M. Mohan, S. Kuppusamy, P. K. Chinaraga, M. Muthurathinam, C. V. S. B. Rao, S. Nagarajan and P. Deivasigamani, An azo-receptor immobilized mesoporous honeycomb silica framework as a solid-state chromogenic sensor for capturing ultra-trace cadmium ions from environmental/industrial samples, *J. Mater. Chem. A*, 2024, **12**, 30567–30581.
42 T. Guo, Y. Wang, J. Li, X. Ding, Q. Sun, J. Yuan, L. Ma, H. Hao and B. Zhou, Porous Organic Polymers with Embedded Fe2O3 Nanoparticles for Pathogenic Microorganism Inactivation and Iodine Removal from Nuclear Water, *ACS Appl. Nano Mater.*, 2024, **7**, 17391–17405.
43 X. Ruan, M. Wei, X. He, L. Wang, D. Yang, Y. Cai, J. Shao and X. Dong, Asymmetric aza-BODIPY photosensitizer for photoacoustic/photothermal imaging-guided synergistic photodynamic/photothermal therapy, *Colloids Surf., B*, 2023, **231**, 113547.
44 D. Xu, J. Liu, Y. Wang, Y. Jian, W. Wu and R. Lv, Black Phosphorus Nanosheet with High Thermal Conversion Efficiency for Photodynamic/Photothermal/Immunotherapy, *ACS Biomater. Sci. Eng.*, 2020, **6**, 4940–4948.
45 Q. Guo, R. Xiao, H. Chen, M. Bao, J. Qi, Q.-q. Jia and W. Zhang, Mechanism of TMB Discoloration Catalyzed by Layered CoNi@CN Nanozymes: Application Based on Smart Phone for Resorcinol Detection, *Chin. J. Chem.*, 2025, **43**, 281–291.
46 Y. Bai, W. Gao, J. Wei, B. Yu, L. Zhang, P. Zhu and J. Yu, Biomimetic cascade intelligent paper chip sensor based on bimetallic porphyrin-based covalent organic framework with triple-enzyme mimetic activities, *Chem. Eng. J.*, 2024, **490**, 151628.
47 Y. Chen and G. Yang, Light-Mediated Modulation of Enzyme-Mimetic Activity of CuMnO2 Nanosheets, *J. Phys. Chem. Lett.*, 2022, **13**, 11770–11777.
48 D. Li, C. Lan, B. Chu, L. Meng and N. Xu, FeMo2Ox(OH)y-based mineral hydrogels as a novel POD nanozyme for sensitive and selective detection of aromatic amines contaminants *via* a colorimetric sensor array, *J. Hazard. Mater.*, 2024, **469**, 133918.
49 M. Lv, Z. Xu, Y. Yong, H. Wang, C. Liu, Q. Xu, G. Du, J. Xie, Y. You, J. Xiao and G. Jiang, Polyoxometalate-based heterojunction with NIR light-facilitated photocatalytic W6+/W5+ redox cycling for enhanced bacteria-infected wound healing, *Mater. Des.*, 2023, **226**, 111673.
50 S. Liu, B. Wang, Y. Yu, Y. Liu, Z. Zhuang, Z. Zhao, G. Feng, A. Qin and B. Z. Tang, Cationization-Enhanced Type I and Type II ROS Generation for Photodynamic Treatment of Drug-Resistant Bacteria, *ACS Nano*, 2022, **16**, 9130–9141.
51 K. Wang, Z. Zhang, L. Lin, J. Chen, K. Hao, H. Tian and X. Chen, Covalent Organic Nanosheets Integrated Heterojunction with Two Strategies To Overcome Hypoxic-Tumor Photodynamic Therapy, *Chem. Mater.*, 2019, **31**, 3313–3323.
52 F. Ge, Y. Sun, Y. Wang, D. Yu, Z. Wang, F. Yu, B. Yu and H. Fu, A simple hydrogen peroxide-activatable Bodipy for tumor imaging and type I/II photodynamic therapy, *J. Mater. Chem. B*, 2024, **12**, 11165–11171.
53 Z. Su, Q. Han, F. Zhang, X. Meng and B. Liu, Preparation, characterization and antibacterial properties of 6-deoxy-6-arginine modified chitosan, *Carbohydr. Polym.*, 2020, **230**, 115635.
54 P. Chen, R. Ze, X. Xia, Z. Zhang, K. Lu, L. Wei and B. Zhou, Composite porphyrin-based conjugated microporous polymer/graphene oxide capable of photo-triggered combinational antibacterial therapy and wound healing, *Biomater. Adv.*, 2023, **154**, 213662.
55 Y. Zhan, X. Hu, Y. Li, Y. Wang, H. Chen, C. A. Omolo, T. Govender, H. Li, F. Huang, L. Shi, X. Hu and Y. Liu, Antimicrobial Hybrid Amphiphile *via* Dynamic Covalent Bonds Enables Bacterial Biofilm Dispersal and Bacteria Eradication, *Adv. Funct. Mater.*, 2023, **33**, 2214299.
56 H. Zhang, J. Ma, C. Liu, L. Li, C. Xu, Y. Li, Y. Li and H. Tian, Antibacterial activity of guanidinium-based ionic covalent organic framework anchoring Ag nanoparticles, *J. Hazard. Mater.*, 2022, **435**, 128965.
57 L. Li, J. Ma, Y. Cui, C. Liu, H. Li, D. Xie, T. Wang, Y. Li and Y. Li, The photosensitizer system based on cationic COF carrier with the loading tetraminoporphyrin and its combined antibacterial effect, *New J. Chem.*, 2024, **48**, 14155–14162.
58 S. S. Varankar and S. A. Bapat, Migratory Metrics of Wound Healing: A Quantification Approach for *in vitro* Scratch Assays, *Front. Oncol.*, 2018, **8**, 633.
59 Y. Chen, T. Feng, X. Zhu, Y. Tang, Y. Xiao, X. Zhang, S.-F. Wang, D. Wang, W. Wen, J. Liang and H. Xiong, Ambient Synthesis of Porphyrin-Based Fe-Covalent Organic Frameworks for Efficient Infected Skin Wound Healing, *Biomacromolecules*, 2024, **25**, 3671–3684.
60 Y. Liu, Y. Li, L. Jiao, Y. Kang, B. Du, W. Cai, H. Cui and R. Zhang, Hypoxia-Activated Biodegradable Porphyrin-Based Covalent Organic Frameworks for Photodynamic and Photothermal Therapy of Wound Infection, *ACS Appl. Mater. Interfaces*, 2024, **16**, 65907–65917.